Photo-dynamical characterisation of the K2-138 resonant chain: Estimation of a mass–radius relationship for resonant sub-Neptunes

Citation for the original published paper (version of record):
Leleu, A., Alnajjarine, A., Delisle, J. et al (2026). Photo-dynamical characterisation of the K2-138 resonant chain: Estimation of a mass–radius
relationship for resonant sub-Neptunes. Astronomy and Astrophysics, 711.
http://dx.doi.org/10.1051/0004-6361/202558317

A&A, 711, A221 (2026)
https://doi.org/10.1051/0004-6361/202558317

Astronomy & Astrophysics

Photo-dynamical characterisation of the K2-138 resonant chain

Estimation of a mass–radius relationship for resonant sub-Neptunes*

A. Leleu[1,2,**], A. Alnajjarine[3], J.-B. Delisle[1], A. Brandeker[4], A. C. M. Correia[5], S. G. Sousa[6,7], T. G. Wilson[8], N. Billot[1], C. Broeg[2,9], M. Rosenqvist[1], J. Korth[1], A. Bonfanti[10], C. Pezzotti[11], B. Akinsanmi[1], Y. Alibert[9,2], R. Alonso[12,13], T. Bárczy[14], D. Barrado[15], S. C. C. Barros[6,7], W. Baumjohann[10], W. Benz[2,9], M. Bergomi[16], L. Borsato[16], A. Castro-González[1], A. Collier Cameron[17], C. Corral van Damme[18], Sz. Csizmadia[19], P. E. Cubillos[10,20], M. B. Davies[21], M. Deleuil[22], A. Deline[1], O. D. S. Demangeon[6,7], B.-O. Demory[9,23,2], A. Derekas[24], B. Edwards[25], D. Ehrenreich[1,26], A. Erikson[19], A. Fortier[2,9], L. Fossati[10], M. Fridlund[27,28], D. Gandolfi[29], K. Gazeas[30], M. Gillon[31], M. Güdel[32], M. N. Günther[18], A. Heitzmann[1], Ch. Helling[10,33], K. G. Isaak[18], T. Keller[2,9], L. L. Kiss[34,35], D. Kitzmann[2,9], E. Kopp[36], K. W. F. Lam[19], J. Laskar[3], A. Lecavelier des Etangs[37], M. Lendl[1], A. Luntzer[32], D. Magrin[16], P. F. L. Maxted[38], B. Merín[39], C. Mordasini[2,9], V. Nascimbeni[16], G. Olofsson[4], H. P. Osborn[9,40], R. Ottensamer[32], I. Pagano[41], E. Pallé[12,13], G. Peter[19], D. Piazza[42], G. Piotto[16,43], D. Pollacco[8], D. Queloz[40,44], R. Ragazzoni[16,43], N. Rando[18], H. Rauer[45,46], I. Ribas[47,48], N. C. Santos[6,7], G. Scandariato[41], D. Ségransan[1], A. E. Simon[2,9], A. M. S. Smith[19], M. Stalport[11,31], S. Sulis[22], Gy. M. Szabó[24,49], S. Udry[1], S. Ulmer-Moll[50,11], V. Van Grootel[11], J. Venturini[1], E. Villaver[12,13], and N. A. Walton[51]

(Affiliations can be found after the references)

Received 28 November 2025 / Accepted 11 May 2026

ABSTRACT

Context. The K2-138 system consists of a K-dwarf transited by six planets in the sub-Neptune regime, with radii ranging from 1.5 to 3.4 $R_\oplus$ and orbital periods of between 2.3 and 42 days. The five innermost planets form a chain of zero-order three-body resonances, while the outermost planet is suspected to be linked to the chain through a first-order three-body resonances. The transit timing variations induced by the resonant configuration enable a precise determination of the system's architecture. The fine-tuning and fragility of K2-138 and other resonant chains ensure that no significant scattering or collision event has taken place since the formation and migration of the planets in the protoplanetary disc, and hence provide important anchors for planet formation models.

Aims. We aim to improve the characterisation of the architecture of this system, in particular the planetary masses and its resonant configuration. In addition, we place this system in context with other resonant chains, and expand on the recent finding that resonant sub-Neptunes are puffier than non-resonant ones by deriving a mass-radius relationship for each population.

Methods. We performed a global analysis of all available photometry and radial velocity data for K2-138 using photo-dynamical modelling of the light curve. We also tried different sets of priors on the masses and eccentricity, as well as different stellar activity models, to study their effects on the masses estimated by transit timing variations and radial velocities.

Results. We show that our joint photo-dynamical and radial velocity analysis resulted in a robust mass determination for planets b to f, with a precision of ~15% for the mass of planet f, and better than 10% for planets b to e. We also show that K2-138 is indeed currently locked in the resonant configuration, the five inner planets librating around an equilibrium of the chain; however, existing data are not sufficient to verify if the outer triplet is librating in a first-order three-body resonance. Finally, we demonstrate that the mass-radius relationship of resonant sub-Neptunes is well described by $M = 2.54\,R^{0.84}$, which is less dense than the non-resonant population, for which we found $M = 2.78\,R^{1.32}$. We also found that the resonant population has a smaller spread around its mass-radius relationship than the non-resonant population, pointing towards an inter-system similarity in the composition of the resonant sub-Neptunes.

Key words. methods: data analysis – celestial mechanics – planets and satellites: detection

1. Introduction

The observed architecture of planetary systems, defined as the orbit and composition of their planets, is the outcome of their formation in their proto-planetary disc and long-term evolution (typically gigayears) after its dispersal. A relatively rare type of architecture is called resonant chains. These chains can be made of two types of resonances. Two-body resonant chains have each of their neighbouring pairs of planets captured in a mean-motion resonance (MMR), where their period ratio is close to a rational number of small integers, p and q, such that $P_{n+1}/P_n \sim (p+q)/p$. For three-body resonant chains, it is each consecutive triplet of planets that satisfies $P_{n+2} \sim j/((k+j)/P_{n+1} - k/P_n)$, with k and j small integers. The fine-tuning and fragility of these orbital configurations ensure that no significant scattering or collision event has taken place since the end of the migration of the planets in the disc (e.g. Mills et al. 2016;

* This study uses CHEOPS data observed as part of the guaranteed time observations CH_PR120053 and CH_PR140080.

** Corresponding author: adrien.leleu@unige.ch

Izidoro et al. 2017). Recent studies show that resonant chains differs from the bulk of exoplanet in terms of both the density of the planets, which is typically lower than for non-resonant systems, and the mutual inclination between the planets, which is also smaller than for other multi-planetary systems (Leleu et al. 2024a). While several mechanisms had been proposed to explain these differences (Lee & Chiang 2016; Millholland 2019; Millholland et al. 2024), Leleu et al. (2024a) showed that these two properties (puffier and more coplanar) are a natural outcome of the breaking the chain model (Izidoro et al. 2017), in which close-in systems of sub-Neptunes form in resonant chains due to the migration of planets in the protoplanetary discs and the positive torque at the inner edge of the disc (e.g. Goldreich & Tremaine 1979; Weidenschilling & Davis 1985; Masset et al. 2006; Terquem & Papaloizou 2007). Resonant chains can then become dynamically unstable after the gaseous disc dissipates (Terquem & Papaloizou 2007; Ogihara & Ida 2009; Cossou et al. 2014). This model reproduces the observed period ratio and multiplicity distribution of the close-in sub-Neptune population if $\approx 95\%$ of the chains become unstable after the disc dispersal (Izidoro et al. 2017). Chains made of more massive planets get destabilized faster Leleu et al. (2024a). In addition, some of these instabilities lead to giant impacts that can eject part, or all, the primordial H/He atmospheres of the planets (Biersteker & Schlichting 2019), resulting in non-resonant planets that are on average denser than their resonant counterpart. Resonant chains would therefore be archetypal of the population of close-in sub-Neptune at their birth, a population that is present around 30 to 50% of all Sun-like stars (Lovis et al. 2009; Howard et al. 2012; Fressin et al. 2013).

To date, resonant chains have only been observed for a few systems: GJ 876 (Rivera et al. 2010), Kepler-60 (Goździewski et al. 2016), Kepler-80 (MacDonald et al. 2016), Kepler-223 (Mills et al. 2016), TRAPPIST-1 (Gillon et al. 2017; Luger et al. 2017), K2-138 (Lopez et al. 2019), TOI-178 (Leleu et al. 2021a), TOI-1136 (Dai et al. 2023), and HD 110067(Luque et al. 2023). All these systems, except GJ 876, are transiting, which provides an opportunity to observe the effect of planet-planet gravitational interactions, and thus constrain the masses and eccentricities of the planets via their transit timing variations (TTVs). For stars that are bright enough, it is also possible to obtain radial velocity (RV) measurements, which can provide complementary constraints on the planetary masses and orbital parameters. Out of the transiting systems cited above, RV measurements have only been published for K2-138, TOI-178, TOI-1136, and HD 110067 so far, the other ones being too faint in the visible (V-mag$\gtrsim$14). Having the possibility to measure planetary masses independently from RVs and TTVs is especially valuable to understand how choices of noise models and degeneracies between parameters affect the robustness of mass measurements for each technique. Characterising planetary systems with both techniques has other advantages: the combination enables complementary constraints on the system architecture, such as precise eccentricities from TTVs, a hint of potential non-transiting planets from RVs, and improved precision for the parameters, such as the planetary mass, that are constrained by both methods. Finally, when precise enough, the combination of RVs and TTVs enables absolute mass measurements (i.e. independent on prior knowledge of stellar parameters).

Out of these four resonant chains bright enough for ground-based follow-up, K2-138 has the longest observational baseline in photometry, with K2 data taken in late 2016 and an ongoing monitoring in 2025. The system is made of six transiting sub-Neptunes (Christiansen et al. 2018; Lopez et al. 2019; Hardegree-Ullman et al. 2021; Vivien et al. 2024), with the five inner planets forming a three-body resonant chain with period ratios close to 3 : 2 for planets b to f. Cerioni & Beaugé (2023) showed that planet g was also potentially part of the chain, forming a first-order three-body resonance with planets e and f. If confirmed, this would be the first occurrence of first-order three-body resonance in extrasolar systems. To confirm this resonance, we would need to see its effects on the TTVs of the triplet (e, f, g). However, probably due its relative faintness, no TTV modelling has been performed yet for this target.

In this paper, we combine archival data from K2 (Howell et al. 2014), the High Accuracy Radial velocity Planet Searcher (HARPS, Mayor et al. 2003), with data from the *Transiting Exoplanet Survey Satellite* (TESS, Ricker et al. 2015) published by Lopez et al. (2019), with data from the *Spitzer Space Telescope* (Spitzer, Werner et al. 2004) published by Hardegree-Ullman et al. (2021), and with data from the *CHaracterising ExOPlanets Satellite* (CHEOPS, Benz et al. 2021) published by Vivien et al. (2024). We also use 43 new CHEOPS visits taken from 2022 to 2025. The data analysis, performed by a photo-dynamical fit of all available photometry joint with the fit of available RV measurements, is presented in Sect. 3. In Sect. 4, we then present the result of our analysis. In particular, we discuss the robustness of the extracted masses, and the resonant dynamics of the system, and we derive a mass-radius relationship for resonant sub-Neptunes. Finally, we conclude in Sect. 5.

2. Data

All detrended data are shown in Appendix B.

2.1. K2

K2-138 was observed for 79 days during the campaign 12 of the K2 mission (Howell et al. 2014) between December 15, 2016 and March 04, 2017, then for 7 days during the campaign 19 in September 2018. Campaign 19 was the final campaign of the mission, and only 7 days are available because the spacecraft ran out of fuel[1]. K2 data were downlinked from the spacecraft, processed into calibrated pixel files and photometric time series, and released to the public via the Mikulski Archive for Space Telescopes[2] (MAST). We downloaded the raw sap flux as well as the co-trending basis vectors using the lightkurve package[3].

2.2. CHEOPS

K2-138 was observed by CHEOPS by a Guest Observer programme for 12 visits in 2020 (Vivien et al. 2024). It was then followed by guaranteed time observation programmes from 2022 to 2025. All visits are detailed in Table F.1. The raw data of each visit were reduced with PIPE[4] (Brandeker et al. 2022), a point spread function (PSF) photometry package developed specifically for CHEOPS. PIPE first uses a principal component analysis (PCA) approach to derive a PSF template library from the data series. The first five principal components (PCs) together with a constant background are then used to fit the individual PSFs of each image using a least-squares minimisation and measure the target's flux. The number of PCs to use

[1] https://keplergo.github.io/KeplerScienceWebsite/k2-data-release-notes.html#k2-campaign-19
[2] https://archive.stsci.edu
[3] https://lightkurve.github.io/lightkurve/
[4] https://github.com/alphapsa/PIPE

is a trade-off between following systematic PSF changes and overfitting the noise. For faint stars such as K2-138, the mean PSF (first PC) is sufficient for a good extraction, and attempts to model the PSF better, with more PCs usually introducing noise in the extracted light curve. Some advantages of using PSF photometry rather than aperture photometry for faint targets are that: (1) the contributions to the signal of each pixel over the PSF are weighted according to noise so that higher signal-to-noise (S/N) photometry can be extracted; (2) cosmic rays and bad pixels (both hot and telegraphic) are easier to filter out or give lower weight in the fitting process; (3) PSF photometry is less sensitive to contamination from nearby background stars; and (4) the background is fitted simultaneously with the PSF for the same pixels, which can be an advantage if there is some spatial structure. For each visit, we then filter out all the data for which the background contamination rises above 300 [electrons/pixel/exposure].

2.3. TESS

TESS (Ricker et al. 2015) observed K2-138 with a two-minute cadence in September 2021 (Sector 42) and October 2023 (Sector 70). The data were processed with the TESS Science Processing Operations Center (SPOC) pipeline (Jenkins et al. 2016) at NASA Ames Research Center. We retrieved the 2-minute cadence Pre-search Data Conditioning Simple Aperture Photometry (PDCSAP, Stumpe et al. 2012; Smith et al. 2012; Stumpe et al. 2014) from MAST, using the default-quality bitmask.

2.4. HARPS

Lopez et al. (2019) collected 215 spectra of K2-138 over 79 nights between September 25, 2017 and September 04, 2018 with the HARPS spectrograph (R ∼ 115 000) mounted on the 3.6 m Telescope at ESO La Silla Observatory (Mayor et al. 2003). We downloaded the dates, radial velocities, and indicators on the DACE platform[5] selecting the 3.2.5 DRS (Dumusque et al. 2021). This DRS reduced the number of point to 208. We selected the measurements for which the contrast and full width at half maximum (FWHM) is at less than three sigma from their mean value. This step reduced the number of measurements to 200.

3. Data analysis

3.1. Spectroscopic parameters

The spectroscopic parameters ($T_{\rm eff}$, $\log g$, microturbulence, [Fe/H]) were estimated using the ARES+MOOG methodology. The methodology is described in detail in Sousa et al. (2021); Sousa (2014); Santos et al. (2013). For this we used the latest version of ARES[6] (Sousa et al. 2007, 2015) to consistently measure the equivalent widths (EWs) of selectd iron lines on the combined HARPS spectrum of K2-138. The list of iron lines is the same as the one presented in Sousa et al. (2008). In this analysis we use a minimization process to find the ionization and excitation equilibrium to converge for the best set of spectroscopic parameters. This process makes use of a grid of Kurucz model atmospheres (Kurucz 1993) and the radiative transfer code MOOG (Sneden 1973). We also derived a more accurate trigonometric surface gravity using recent GAIA data following the same procedure as is described in Sousa et al. (2021). These parameters are presented in Table 1.

Table 1. Properties of the host star K2-138, Gaia ID 2413596935442139520.

Property (unit)	Value	Source
Astrometric properties		
RA (J2000)	348.95 ± 0.01	[1]
Dec (J2000)	-10.85 ± 0.01	[1]
$\mu_{\rm RA}$ (mas yr^{-1})	1.079 ± 0.017	[1]
$\mu_{\rm Dec}$ (mas yr^{-1})	-10.675 ± 0.0150	[1]
Parallax (mas)	4.9138 ± 0.0150	[1]
Distance (pc)	203.5 ± 0.6	from parallax
Photometric magnitudes		
G (mag)	12.022 ± 0.003	[1]
$G_{\rm BP}$ (mag)	12.438 ± 0.003	[1]
$G_{\rm RP}$ (mag)	11.443 ± 0.004	[1]
J (mag)	10.756 ± 0.021	[2]
H (mag)	10.384 ± 0.021	[2]
K (mag)	10.305 ± 0.021	[2]
$W1$ (mag)	10.274 ± 0.023	[3]
$W2$ (mag)	10.332 ± 0.019	[3]
Spectroscopic and derived properties		
$T_{\rm eff}$ (K)	5275 ± 67	Spectroscopy [4]
$\log g_\star$ (cgs)	4.51 ± 0.03	Spec + Trig [4]
$\log g_\star$ (cgs)	4.34 ± 0.12	Spectroscopy [4]
[Fe/H] (dex)	0.06 ± 0.05	Spectroscopy [4]
$v \sin i_\star$ (km s^{-1})	3.3 ± 0.5	Spectroscopy [4]
$R_\star$ ($R_\odot$)	0.845 ± 0.006	IRFM [4]
$M_\star$ ($M_\odot$)	0.862 ± 0.034	Isochrones [4]
$t_\star$ (Gyr)	7.8 ± 2.7	Isochrones [4]
$L_\star$ ($L_\odot$)	0.496 ± 0.026	from $R_\star$ and $T_{\rm eff}$ [4]
$\rho_\star$ ($\rho_\odot$)	1.429 ± 0.064	from $R_\star$ and $M_\star$ [4]
P_{rot} (day)	24.7 ± 2.2	[5]

Notes. [1] *Gaia* EDR3 (Gaia Collaboration 2021); [2] 2MASS (Skrutskie et al. 2006); [3] WISe (Wright et al. 2010); [4] this work; [5] (Lopez et al. 2019).

Using our stellar spectral parameters derived above and observed broadband fluxes and uncertainties retrieved from the most recent data releases in the following bandpasses: *Gaia* G, $G_{\rm BP}$, and $G_{\rm RP}$, 2MASS J, H, and K, and *WISE* W1 and W2 (Skrutskie et al. 2006; Wright et al. 2010; Gaia Collaboration 2023), we determined the stellar radius via a Markov chain Monte Carlo infrared flux method (Blackwell & Shallis 1977; Schanche et al. 2020). By constraining stellar atmospheric models with our $T_{\rm eff}$, $\log g$, and [M/H] we produced synthetic photometry in the *Gaia*, 2MASS, and *WISE* bandpasses that were compared to the broadband photometry to obtain the stellar angular diameter, which was converted to the stellar radius using the *Gaia* DR3 offset-corrected parallax (Lindegren et al. 2021). To account for uncertainties in stellar atmospheric modeling, we conducted a Bayesian modelling averaging of the posterior distributions from the individual ATLAS (Kurucz 1993; Castelli & Kurucz 2003) and PHOENIX (Allard 2014) catalogues to produce a value of $R_\star = 0.845 \pm 0.006\, R_\odot$.

Adopting $T_{\rm eff}$, [M/H], and $R_\star$ as input parameters, we finally derived the stellar mass, $M_\star$, and age, $t_\star$, using two different sets of stellar evolutionary models. The first pair of mass

[5] https://dace.unige.ch/radialVelocities/?pattern=K2-138

[6] The last version, ARES v2, can be downloaded at https://github.com/sousasag/ARES

and age estimates was computed via the isochrone placement algorithm (Bonfanti et al. 2015, 2016), which interpolates the input values within pre-computed grids of PARSEC[7] v1.2S (Marigo et al. 2017) isochrones and evolutionary tracks. We also derived a second pair of mass and age values by employing the CLES (Code Liégeois d'Évolution Stellaire; Scuflaire et al. 2008) code, which generates the best-fit evolutionary track following the Levenberg-Marquadt minimisation scheme as outlined in Salmon et al. (2021). After checking the consistency of the two respective pairs of outcomes via the χ^2-based criterion described in Bonfanti et al. (2021), we finally merged our results and we obtained $M_\star = 0.862 \pm 0.034\, M_\odot$ and $t_\star = 7.8 \pm 2.7$ Gyr.

3.2. Approach

The TTVs expected for K2-138 were discussed in Christiansen et al. (2018) and Lopez et al. (2019). In both publications, the expected amplitude is less than 10 minutes for the five inner planets, with a period of ∼145 days. However these estimations were performed using the `TTVFaster` code (Agol & Deck 2016), which is based on an analytical model that is valid only outside of MMRs. Two-body and three-body MMRs can generate much larger TTVs on longer timescales (e.g. Nesvorný & Vokrouhlický 2016; Agol et al. 2020; Leleu et al. 2024b).

Transit timing variations can be studied by pre-extracting all the transit timings of the planets, then fitting these transit timings. Alternatively, one can analyse TTVs using a photo-dynamical model (Ragozzine & Holman 2010; Carter et al. 2012; Masuda & Tamayo 2020; Leleu et al. 2023; Korth et al. 2024), in which the ideal light curve, accounting for TTVs, is modelled and then fit to the data. Leleu et al. (2023) showed that photo-dynamical analysis often allows for a more robust mass estimate, especially for systems harbouring planets whose individual transit S/N is low (typically ≲3.5). Here, the standard deviation of the TESS 2-min cadence data is of 0.0023. Considering a transit depth of ∼300 ppm and a transit duration of 2 hours for K2-138, the S/N of its individual transits is below one. We therefore performed a photo-dynamical analysis of the data.

The TTV characterisation of multi-planetary systems can be affected by two layers of eccentricity degeneracies: a degeneracy between the mass of the planets and the part of the eccentricities related to the resonant interaction (Boué et al. 2012; Lithwick et al. 2012), and the degeneracy of the non-resonant part of the eccentricities (Leleu et al. 2021a). To check the robustness of the masses we derived, we followed the same steps as in Leleu et al. (2023, 2024b): we tried out a set of priors that pulls the solution toward opposite directions of the degeneracy. We used the 'default' and 'high-mass' sets of priors of Hadden & Lithwick (2017): the default prior is log-uniform in planet mass and uniform in eccentricity, while the high-mass prior is uniform in planet mass and log-uniform in eccentricity. In addition, following Leleu et al. (2023), we performed a third fit, using log-uniform mass prior and the Kipping (2013) prior for the eccentricity: a β distribution of parameters $\alpha = 0.697$ and $\beta = 3.27$. The posterior associated with this set of priors is referred to as the 'final' posterior. Then, following Leleu et al. (2023), we quantified the robustness of the mass determination by studying the difference between the mass posteriors using the quantity Δ_M:

$$\Delta_M = \max(\Delta_{M+}, \Delta_{M-}), \tag{1}$$

which estimates the departure of the median of the 'default' and 'high-mass' posteriors from the final posterior. More precisely,

$$\Delta_{M+} = \frac{m_{max,0} - m_{final,0}}{m_{final,+\sigma} - m_{final,0}}, \tag{2}$$

where $m_{max,0}$ is the maximum between the medians of the 'default' and 'high-mass' posterior, $m_{final,0}$ is the median of the 'final' posterior, and $m_{final,+\sigma}$ is the 0.84 quantile of the 'final' posterior. $\Delta_{M+} = 0$ if $m_{max,0} < m_{final,0}$.

$$\Delta_{M-} = \frac{m_{final,0} - m_{min,0}}{m_{final,0} - m_{final,-\sigma}}, \tag{3}$$

where $m_{min,0}$ is the minimum of the 'default' and 'high-mass' posterior medians, and $m_{final,-\sigma}$ is the 0.16 quantile of the final posterior. $\Delta_{M-} = 0$ if $m_{min,0} > m_{final,0}$. The values of Δ_M obtained for each planet are given in Tables 2 and 3, and discussed in Sect. 4.2.

3.3. Data modelling

We performed a joint analysis of all available transit events as well as the RV data. The gravitational interaction of the six planets was also taken into account. For these planets, we used wide, flat priors for the mean longitude, period, impact parameter, and ratio of the radius of the planet over the radius of the star, $R_p/R_\star$. The mass and $e\cos\varpi$ and $e\sin\varpi$ priors are given in Sect. 3.2. The stellar density and stellar radius have Gaussian priors, with the values given in Table 1.

3.3.1. Photometry

The photo-dynamical model of the planetary signals, presented in detail in Leleu et al. (2021b, 2023), was computed by predicting transit timings using the `TTVfast` package (Deck et al. 2014) of the six planets, and modelling the transits of each planet using the `batman` package Kreidberg (2015). We modelled the instrumental systematics as well as stellar activity using a linear combination of indicators and B-splines. We used B-splines as functions of time for all photometric data, and an additional B-spline was added with respect to the roll-angle for each CHEOPS visit. The temporal B-splines have nodes separated by 0.4 days for all photometry, and the periodic B-splines on the roll angle for CHEOPS have nodes separated by 0.1 radians. For K2 we used the 16 co-trending basis vectors. For CHEOPS, we used as indicators the telescope tube temperature, the position of the centroid along the Y direction, and the background contamination. For the Spitzer data, we used the pre-detrended light curve from Hardegree-Ullman et al. (2021). For TESS, we used the PDC-SAP flux that had already removed the instrumental effect, so no indicators were used. This model (indicators and B-splines) only introduces linear parameters. To accelerate the exploration of the parameter space, we computed the likelihood marginalized over these linear parameters, using the `linmarg`[8] python package (Leleu et al. 2023). The limb-darkening parameters have Gaussian priors computed by LDCU (Deline et al. 2022) for each photometric instrument. In addition, a jitter term was added for each instrument with a flat prior.

3.3.2. Radial velocities

The RV model of the planetary signals was also computed using the `TTVfast` package (Deck & Agol 2016). We fitted these

[7] *PA*dova and *TR*ieste *S*tellar *E*volutionary *C*ode: http://stev.oapd.inaf.it/cgi-bin/cmd

[8] https://gitlab.unige.ch/delisle/linmarg

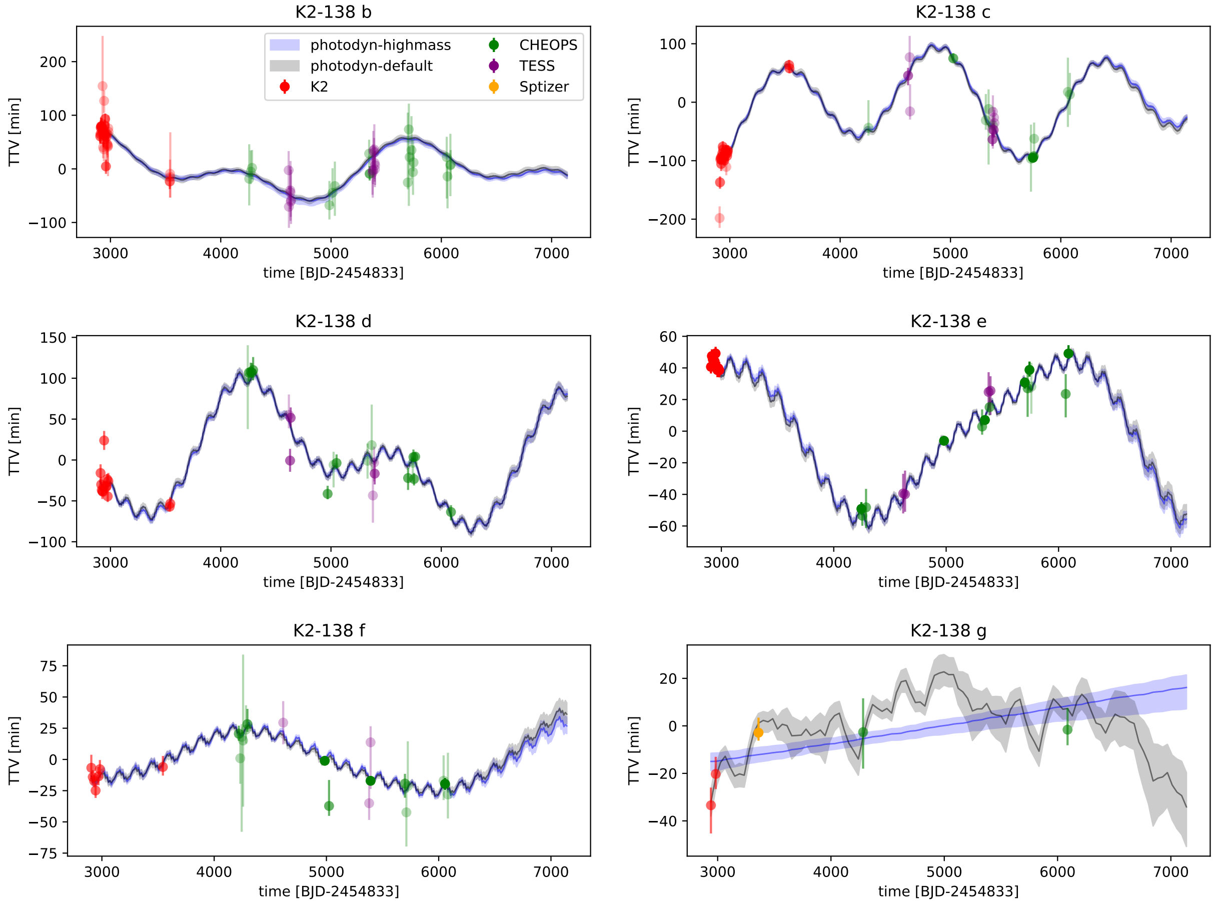

Fig. 1. Transit timing variations for the six planets of K2-138. The filled area corresponds to the 1σ posterior of the photo-dynamical fits presented in Sect. 3.2. The error bars show an estimation of the 1σ interval for the mid-transit timing of individual transits for each instrument.

data by modelling the planets' orbits as well as stellar activity using a Gaussian process (GP) model trained simultaneously on the RVs, FWHM, and contrast, using the `spleaf`[9] package. The time series and the posterior of the RV fit are shown in Fig. C.2. The periodograms of the activity indicators are shown in Fig. C.3. We used a data-driven FENRIR kernel, with a single-mode, two-harmonics, Matérn 1/2 decay at the rotation period of the star, and a single-mode Matérn 1/2 decay for the (super)-granulation (see Appendix C and Hara & Delisle (2025) for more details).

4. Results of the data analysis

The transit timings estimated for each planet, as well as 300 samples of the final posterior, can be found online. In particular, the transit timings are propagated until 2030, to be usable for follow-up observations of the system.

4.1. Recovered TTV signal

Figure 1 shows the modeled TTVs for the six planets of K2-138. The filled grey and blue areas correspond to the 1σ interval for the posterior of the default and high-mass sets of priors, respectively. The points with error bars correspond to the fit of individual transit times. Given the low S/N of individual transits, strong outliers are expected (e.g. Agol et al. 2020). One can see that the photo-dynamical models' timings are better constrained than the individual timings, highlighting the need for photo-dynamical modeling for low-S/N TTV analysis.

The recovered TTVs of planets c to f show the expected signal with a period of 145 days, which is the super-period defined by the distance to the neighbouring 3:2 MMRs $(1/(2/P_{in} - 3/P_{out}))$. However, its amplitude is quite small : $\lesssim$ 10 min as estimated by Christiansen et al. (2018) and Lopez et al. (2019). Instead, the TTVs are dominated by the libration in the resonant chain, which results in TTVs of peak-to-peak amplitudes of several tens, up to two hundreds of minutes, over 9 years. The two sets of priors agree for the TTVs of planets b to f. For planet g, the two analysis disagree, the high-mass prior librating in the first-order three-body MMR, while the angle circulate in the default posterior. This is discussed further in Sect. 4.4.

4.2. Robustness of retrieved masses

To estimate the robustness of mass determination with each technique, we performed RV fits, photo-dynamical fits, and joint fits with the sets of priors defined in Sect. 3.2. Note that for the RV fit the eccentricity of the planets was set to zero, and therefore the default and final sets of prior are identical. For the RV fits, we additionally tested several activity models (see Appendix C), as the choice of model might have an impact on the mass determination (e.g. Bonfils et al. 2018; Ahrer et al. 2021).

We show in Fig. 2, a summary of the mass posteriors from these analyses. The RV mass determination (black) is robust for

[9] https://gitlab.unige.ch/delisle/spleaf

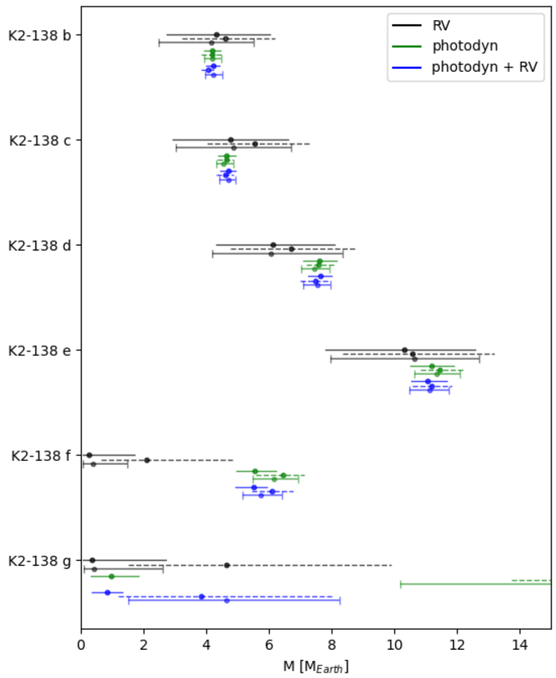

Fig. 2. Mass determination for different datasets and choices of priors. In black are the posterior from the RV analysis with the FENRIR rotation: one mode – three harmonics super granulation; two modes – Matérn 1/2 model (see Appendix C). The green posteriors are from the photo-dynamical model alone, while the blue posteriors are from the joint photo-dynamical and RV fits. The default (1-sigma interval, solid), high-mass (1-sigma, dashed), and final (error bar) sets of priors are defined in Sect. 3.2. The photodyn *final* and photodyn+RV *final* are the cases reported in Tables 2 and 3.

the four inner planets, in the sense that the posteriors for the default and the high-mass priors agree well. The masses of the two outer planets are more sensitive to the choice of priors. We also note that these planets' masses are also more sensitive to a change in the stellar activity model (see Appendix C). We recall that the stellar rotation period was estimated to be about 25 d by Lopez et al. (2019), which is roughly twice the period of K2-138 f. Since we noticed a strong model sensitivity for the two outer planets' masses, we selected the activity model that exhibited large uncertainties for these two parameters for the subsequent analyses (joint fit), in order to avoid biasing the final mass estimates for these planets (see Sect. 3.3.2 and Appendix C). This does not mean that the chosen activity model is intrinsically better, and better constraining the activity model and the planets' masses from RV would require more measurements.

The posteriors of the masses from the photo-dynamical fit for the different sets of priors are shown in green in Fig. 2. As is explained in Sect. 3.2, the Δ_M criterion quantifies the prior-dependency of these masses. $\Delta_M = 0$ indicates that the posteriors of the default, high-mass, and final fit all perfectly agree, while $\Delta_M = 1$ indicates that the median of the default or high-mass posteriors lies exactly at $1 - \sigma$ from the median of the final posterior. Leleu et al. (2023) set an arbitrary limit at $\Delta_M = 1.3$ to estimate if the retrieved mass was degenerate or not. From the photo-dynamical fit alone, planets b to f have robust masses, with values of $\Delta_M \lesssim 0.55$, while the mass of planet g is not constrained by the photo-dynamical model, with $\Delta_M > 5$ (see Tables 2 and 3).

Our RV mass posteriors are given in Table C.1 for the chosen activity model. The median of the Lopez et al. (2019) posterior lies within $\lesssim 1\sigma$ of our confidence interval for planets b to e, while planets f and g are less consistent. Our RV and photo-dynamical masses are also in good agreement for planets b to e. As has been mentioned, for these planets the photo-dynamical masses are robust to the choice of prior. For these planets, the mass recovered in RV is consistent across a test of 18 different mass priors and activity models; see Appendix C. On the contrary, the agreement between photo-dynamical masses and RV masses breaks for the planets that are either not robust in RVs (planets f and g) and/or robust in the photo-dynamical analysis (planet g). Given that we measured consistent masses for b to e with two independent methods (photo-dynamics and RVs), we can consider that these masses are measured accurately. The correlation between accuracy and the robustness checks performed on photo-dynamics and RVs highlights the need to perform such checks systematically.

When looking at the posteriors of the joint fit, in blue in Fig. 2, we can see that most of the constraints on the mass come from the photo-dynamical model, as the joint mass posteriors (green) remain close to the photo-dynamical posteriors (blue). We nonetheless note a general improvement in the robustness of the determined mass, as the prior dependency (Δ_M in Tables 2 and 3) is generally smaller in the joint fit than in the photo-dynamical fit alone, besides a slight increase to $\Delta_M = 0.32$ for K2-138 b. We therefore use the joined analysis *final* posterior for the rest of the paper.

4.3. Recovered planetary parameters

The fitted and derived planetary parameters of K2-138 are listed in Tables 2 and 3. With now 14 planets in resonant chains with a mass precision better than 20% (Mills et al. 2016; Leleu et al. 2023, 2024b, and this work), and 9 with precisions in the 20–40% range (Mills et al. 2016; Luque et al. 2023; Beard et al. 2024), we can fit a mass-radius relationship for the sub-population of resonant (sub-)Neptunes. Using these planets in the [1.5–5] $R_\oplus$ range, we assume that the mass-radius relationship of sub-Neptunes follow a function the form $\log(M) = a\log(R) + b$ plus a spread parameter, σ. We fitted this model to the natural logarithm of the mass and radius of all planets, as well as their error; see Appendix E. This provides both the estimation of the mean values of a, b, and σ, as well as their covariance. We obtained

$$M_{res} = 2.54\,R^{0.84}\left(1 \pm \sqrt{0.05(\log R)^2 - 0.09\log R + 0.10}\right), \quad (4)$$

shown in red in Fig. 3.

We then performed the same computation on the non-resonant multi-planetary and single-planet sample from Leleu et al. (2024a). We obtained

$$M_{non-res}{=}2.78\,R^{1.32}\left(1{\pm}\sqrt{0.034(\log R)^2 + -0.066\log R + 0.19}\right), \quad (5)$$

shown in black in Fig. 3. Given the inhomogeneity in the spread of masses for the non-resonant population in this range of radius, the shape of the law might be too simplistic for this sub-population. Nonetheless, having an identical model for the two populations allows us to compare them directly. We find results in good agreement with those of Leleu et al. (2024a): the resonant population is less dense, and the spread of the resonant population is smaller. This implies an inter-resonant chain

Table 2. Fitted and derived properties of the planets of K2-138

Parameter	Prior	Photo-dynamical	Photo-dynamical + RV
		K2-138b	
λ (deg)	$\mathcal{U}$(–360.00,360.00)	$44.32^{+0.48}_{-0.58}$	$44.35^{+0.40}_{-0.43}$
P (days)	$\mathcal{U}$(2.28,2.42)	$2.353179^{+6.5e-05}_{-8.0e-05}$	$2.353173^{+5.5e-05}_{-7.4e-05}$
$e\cos\varpi$	*	$7.4e-05^{+0.0039}_{-0.0029}$	$-2.9e-04^{+0.0020}_{-0.0023}$
$e\sin\varpi$	*	$0.0017^{+0.0066}_{-0.0019}$	$0.0016^{+0.0049}_{-0.0020}$
$M/M_{\odot}$	*	$1.3e-05^{+8.4e-07}_{-8.6e-07}$	$1.3e-05^{+8.6e-07}_{-8.2e-07}$
$R/R_{\star}$	$\mathcal{U}$(0.0e+00,2.0e-01)	$0.01680^{+6.4e-04}_{-6.5e-04}$	$0.01668^{+6.1e-04}_{-5.2e-04}$
b	$\mathcal{U}$(0.0e+00,8.5e-01)	$0.20^{+0.13}_{-0.13}$	$0.20^{+0.13}_{-0.13}$
dF (ppm)	derived	$282.4^{+22.1}_{-21.5}$	$278.3^{+20.6}_{-17.0}$
e	derived	$0.0045^{+0.0058}_{-0.0037}$	$0.0017^{+0.0024}_{-0.0011}$
ϖ (deg)	derived	66^{+60}_{-105}	82^{+59}_{-146}
I (deg)	derived	$88.64^{+0.91}_{-0.93}$	$88.65^{+0.86}_{-0.91}$
$M(M_{\rm Earth})$	derived	$4.21^{+0.28}_{-0.29}$	$4.23^{+0.29}_{-0.27}$
$R(R_{\rm Earth})$	derived	$1.552^{+0.060}_{-0.058}$	$1.541^{+0.056}_{-0.048}$
$\rho(\rho_{\rm Earth})$	derived	$1.12^{+0.17}_{-0.12}$	$1.14^{+0.16}_{-0.10}$
Δ_M		0.08	0.63
		K2-138c	
λ (deg)	$\mathcal{U}$(–360.00,360.00)	$186.64^{+0.27}_{-0.32}$	$186.62^{+0.18}_{-0.26}$
P (days)	$\mathcal{U}$(3.45,3.67)	$3.55964^{+1.6e-04}_{-1.3e-04}$	$3.55963^{+1.3e-04}_{-1.2e-04}$
$e\cos\varpi$	*	$4.6e-04^{+0.0031}_{-0.0011}$	$4.6e-04^{+0.0022}_{-0.0008}$
$e\sin\varpi$	*	$-3.6e-05^{+0.0020}_{-0.0026}$	$-3.2e-04^{+0.0011}_{-0.0024}$
$M/M_{\odot}$	*	$1.4e-05^{+1.0e-06}_{-6.5e-07}$	$1.4e-05^{+6.9e-07}_{-8.5e-07}$
$R/R_{\star}$	$\mathcal{U}$(0.0e+00,2.0e-01)	$0.02391^{+5.4e-04}_{-6.4e-04}$	$0.02394^{+4.7e-04}_{-5.4e-04}$
b	$\mathcal{U}$(0.0e+00,8.5e-01)	$0.22^{+0.08}_{-0.11}$	$0.22^{+0.09}_{-0.11}$
dF (ppm)	derived	$571.5^{+26.2}_{-30.3}$	$573.3^{+22.5}_{-25.5}$
e	derived	$0.0025^{+0.0032}_{-0.0021}$	$1.0e-03^{+0.0020}_{-0.0007}$
ϖ (deg)	derived	$-8.9^{+85.9}_{-90.5}$	$-33.1^{+95.7}_{-65.4}$
I (deg)	derived	$88.89^{+0.59}_{-0.46}$	$88.87^{+0.58}_{-0.48}$
$M(M_{\rm Earth})$	derived	$4.54^{+0.34}_{-0.22}$	$4.72^{+0.23}_{-0.28}$
$R(R_{\rm Earth})$	derived	$2.206^{+0.051}_{-0.054}$	$2.209^{+0.043}_{-0.045}$
$\rho(\rho_{\rm Earth})$	derived	$0.426^{+0.044}_{-0.035}$	$0.436^{+0.044}_{-0.036}$
Δ_M		0.34	0.38
		K2-138d	
λ (deg)	$\mathcal{U}$(–360.00,360.00)	$87.68^{+0.20}_{-0.19}$	$87.68^{+0.16}_{-0.12}$
P (days)	$\mathcal{U}$(5.24,5.57)	$5.40465^{+2.0e-04}_{-1.7e-04}$	$5.40470^{+1.5e-04}_{-1.6e-04}$
$e\cos\varpi$	*	$-1.5e-06^{+0.0012}_{-0.0015}$	$1.1e-05^{+0.0008}_{-0.0012}$
$e\sin\varpi$	*	$4.9e-06^{+0.0016}_{-0.0014}$	$4.0e-05^{+0.0015}_{-0.0011}$
$M/M_{\odot}$	*	$2.2e-05^{+1.4e-06}_{-1.3e-06}$	$2.3e-05^{+1.3e-06}_{-1.3e-06}$
$R/R_{\star}$	$\mathcal{U}$(0.0e+00,2.0e-01)	$0.02745^{+4.8e-04}_{-5.9e-04}$	$0.02737^{+5.1e-04}_{-5.1e-04}$
b	$\mathcal{U}$(0.0e+00,8.5e-01)	$0.22^{+0.10}_{-0.13}$	$0.21^{+0.09}_{-0.12}$
dF (ppm)	derived	$753.3^{+26.6}_{-32.0}$	$749.0^{+28.0}_{-27.8}$
e	derived	$0.0015^{+0.0024}_{-0.0012}$	$7.0e-04^{+9.1e-04}_{-4.4e-04}$
ϖ (deg)	derived	4^{+97}_{-130}	23^{+107}_{-141}
I (deg)	derived	$89.17^{+0.51}_{-0.41}$	$89.19^{+0.46}_{-0.37}$
$M(M_{\rm Earth})$	derived	$7.46^{+0.48}_{-0.42}$	$7.55^{+0.42}_{-0.44}$
$R(R_{\rm Earth})$	derived	$2.537^{+0.047}_{-0.061}$	$2.527^{+0.054}_{-0.054}$
$\rho(\rho_{\rm Earth})$	derived	$0.459^{+0.042}_{-0.035}$	$0.466^{+0.041}_{-0.038}$
Δ_M		0.30	0.21

Notes. The orbital elements are given at the date 2458352.55018382 BJD. λ is the mean longitude of the planet, ϖ its longitude of periastron. Δ_M is the robustness criterion defined in Equation (1). b, e, M and R are the planet's impact parameter, eccentricity, mass and radius respectively. $M_{\odot}$ is the mass of the sun and $R_{\star}$ is the radius of the star. * The mass and eccentricity priors depend on the case, see Section 3.2.

Table 3. Fitted and derived properties of the planets of K2-138.

Parameter	Prior	Photo-dynamical	Photo-dynamical + RV
		K2-138e	
λ (deg)	$\mathcal{U}$(–360.00,360.00)	$322.72^{+0.20}_{-0.13}$	$322.75^{+0.17}_{-0.15}$
P (days)	$\mathcal{U}$(8.01,8.51)	$8.26292^{+2.0e-04}_{-1.8e-04}$	$8.26301^{+1.7e-04}_{-2.1e-04}$
$e\cos\varpi$	*	$-2.5e-04^{+0.0012}_{-0.0017}$	$-5.3e-04^{+0.0011}_{-0.0012}$
$e\sin\varpi$	*	$-0.0054^{+0.0042}_{-0.0036}$	$-0.0065^{+0.0039}_{-0.0028}$
$M/M_\odot$	*	$3.4e-05^{+2.2e-06}_{-2.1e-06}$	$3.3e-05^{+1.8e-06}_{-1.9e-06}$
$R/R_\star$	$\mathcal{U}$(0.0e+00,2.0e-01)	$0.03612^{+5.3e-04}_{-5.7e-04}$	$0.03606^{+5.0e-04}_{-4.6e-04}$
b	$\mathcal{U}$(0.0e+00,8.5e-01)	$0.504^{+0.026}_{-0.029}$	$0.498^{+0.030}_{-0.022}$
dF (ppm)	derived	$1304.5^{+38.3}_{-40.8}$	$1300.7^{+36.4}_{-32.9}$
e	derived	$0.0055^{+0.0037}_{-0.0038}$	$0.0029^{+0.0025}_{-0.0017}$
ϖ (deg)	derived	$-93.4^{+23.4}_{-15.2}$	$-94.9^{+13.3}_{-13.4}$
I (deg)	derived	$88.52^{+0.10}_{-0.09}$	$88.55^{+0.08}_{-0.11}$
$M(M_{\rm Earth})$	derived	$11.36^{+0.74}_{-0.70}$	$11.13^{+0.60}_{-0.64}$
$R(R_{\rm Earth})$	derived	$3.342^{+0.046}_{-0.064}$	$3.330^{+0.054}_{-0.048}$
$\rho(\rho_{\rm Earth})$	derived	$0.306^{+0.026}_{-0.027}$	$0.301^{+0.021}_{-0.023}$
Δ_M		0.23	0.12
		K2-138f	
λ (deg)	$\mathcal{U}$(–360.00,360.00)	$62.11^{+0.23}_{-0.15}$	$62.16^{+0.21}_{-0.12}$
P (days)	$\mathcal{U}$(12.37,13.14)	$12.76046^{+5.6e-04}_{-6.8e-04}$	$12.76098^{+2.9e-04}_{-3.8e-04}$
$e\cos\varpi$	*	$-3.0e-04^{+0.0010}_{-0.0022}$	$-6.8e-04^{+0.0009}_{-0.0022}$
$e\sin\varpi$	*	$4.2e-04^{+0.0035}_{-0.0012}$	$2.7e-04^{+0.0027}_{-0.0013}$
$M/M_\odot$	*	$1.8e-05^{+2.3e-06}_{-2.0e-06}$	$1.7e-05^{+2.0e-06}_{-1.8e-06}$
$R/R_\star$	$\mathcal{U}$(0.0e+00,2.0e-01)	$0.03071^{+6.5e-04}_{-6.5e-04}$	$0.03075^{+5.1e-04}_{-6.1e-04}$
b	$\mathcal{U}$(0.0e+00,8.5e-01)	$0.593^{+0.020}_{-0.022}$	$0.590^{+0.018}_{-0.016}$
dF (ppm)	derived	$942.9^{+40.6}_{-39.5}$	$945.3^{+31.4}_{-37.1}$
e	derived	$0.0021^{+0.0030}_{-0.0016}$	$0.0014^{+0.0017}_{-0.0009}$
ϖ (deg)	derived	61^{+71}_{-194}	86^{+61}_{-225}
I (deg)	derived	$88.702^{+0.063}_{-0.058}$	$88.710^{+0.046}_{-0.055}$
$M(M_{\rm Earth})$	derived	$6.16^{+0.77}_{-0.66}$	$5.75^{+0.68}_{-0.60}$
$R(R_{\rm Earth})$	derived	$2.839^{+0.062}_{-0.069}$	$2.842^{+0.053}_{-0.061}$
$\rho(\rho_{\rm Earth})$	derived	$0.273^{+0.032}_{-0.039}$	$0.253^{+0.033}_{-0.031}$
Δ_M		0.92	0.53
		K2-138g	
λ (deg)	$\mathcal{U}$(–360.00,360.00)	$139.77^{+0.39}_{-1.13}$	$139.72^{+0.65}_{-1.25}$
P (day)	$\mathcal{U}$(40.71,43.22)	$41.97509^{+4.0e-04}_{-4.1e-04}$	$41.97490^{+3.7e-04}_{-3.9e-04}$
$e\cos\varpi$	*	$0.0019^{+0.0094}_{-0.0036}$	$0.002^{+0.011}_{-0.006}$
$e\sin\varpi$	*	$-3.0e-04^{+0.008}_{-0.017}$	$-9.8e-05^{+0.011}_{-0.012}$
$M/M_\odot$	*	$9.5e-05^{+1.0e-04}_{-6.4e-05}$	$1.4e-05^{+1.1e-05}_{-9.4e-06}$
$R/R_\star$	$\mathcal{U}$(0.0e+00,2.0e-01)	$0.0304^{+0.0012}_{-0.0013}$	$0.0305^{+0.0012}_{-0.0011}$
b	$\mathcal{U}$(0.0e+00,8.5e-01)	$0.736^{+0.018}_{-0.020}$	$0.731^{+0.019}_{-0.017}$
dF (ppm)	derived	$925.9^{+75.0}_{-74.9}$	$928.5^{+72.7}_{-67.0}$
e	derived	$0.009^{+0.020}_{-0.008}$	$0.005^{+0.012}_{-0.004}$
ϖ (deg)	derived	-23^{+124}_{-59}	-5^{+102}_{-80}
I (deg)	derived	$89.272^{+0.026}_{-0.027}$	$89.278^{+0.024}_{-0.025}$
$M(M_{\rm Earth})$	derived	$31.5^{+33.8}_{-21.3}$	$4.65^{+3.62}_{-3.14}$
$R(R_{\rm Earth})$	derived	$2.81^{+0.11}_{-0.12}$	$2.81^{+0.11}_{-0.10}$
$\rho(\rho_{\rm Earth})$	derived	$1.51^{+1.57}_{-1.07}$	$0.20^{+0.18}_{-0.13}$
Δ_M		1.43	1.22

Notes. The orbital elements are given at the date 2458352.55018382 BJD. λ is the mean longitude of the planet, ϖ its longitude of periastron. Δ_M is the robustness criterion defined in Equation (1). b, e, M and R are the planet's impact parameter, eccentricity, mass and radius respectively. $M_\odot$ is the mass of the sun and $R_\star$ is the radius of the star. * The mass and eccentricity priors depend on the case, see Section 3.2.

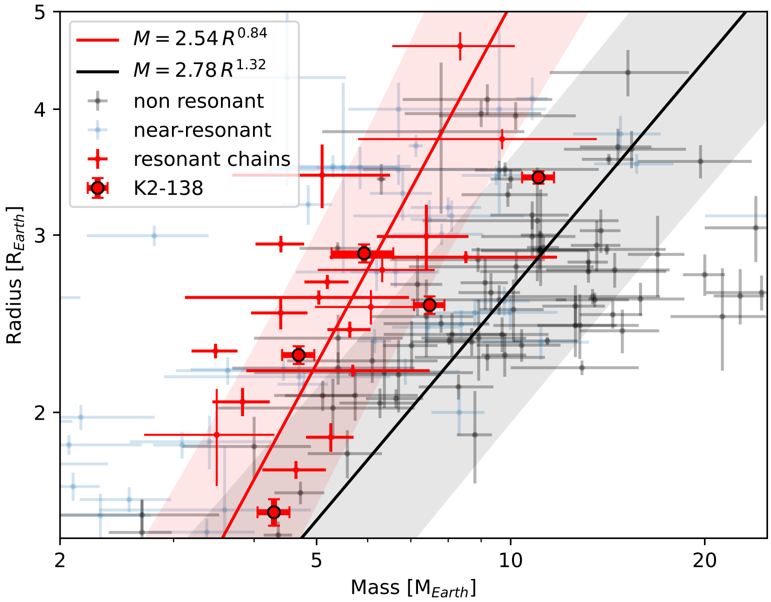

Fig. 3. Mass–radius relationship of known exoplanets with a mass precision better than 40% from the NASA Exoplanet Archive. For planets whose mass was derived by TTVs, only planets that passed the robustness tests similar to the one described in Sect. 3.2 were selected; see Leleu et al. (2024a). Following Leleu et al. (2024a), the near-resonant population, in blue, is defined by $0.002 < \Delta_{MMR} < 0.05$, while single planets are regrouped with non-resonant pairs ($\Delta_{MMR} > 0.05$) and shown in black. The resonant chains masses and radii come from Mills et al. (2016) for Kepler-223, Leleu et al. (2023) for Kepler-60, Leleu et al. (2024b) for TOI-178, Beard et al. (2024) for TOI-1136, Luque et al. (2023) for HD 110067, and this work for K2-138. The red and black lines show a similar log-log law fitted to the resonant chain and non-resonant population, respectively. The respective shaded areas show the spread around that law. See the text for more details.

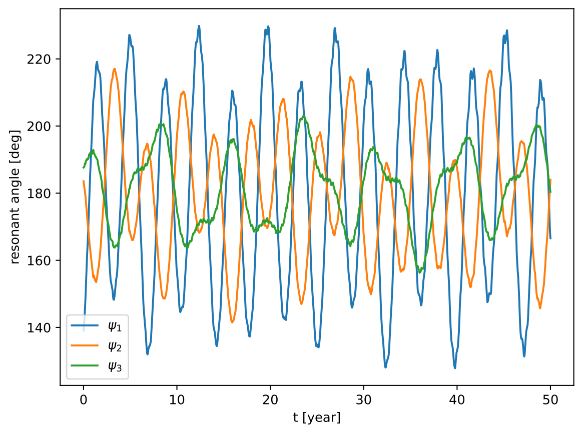

Fig. 4. Evolution of the three-body angles Ψ_1, Ψ_2, and Ψ_3 (Eq. (7)) over 50 years for the final posterior of the photo-dynamical fit. The observational baseline used in this study covers the first 10 years.

similarity in density, and hence possibly in composition, greater than between the non-resonant planets. As an example, on a linear scale, for a 3 $R_\oplus$ planet our mass-radius relations give $M = 6.41^{+1.8}_{-1.4}\ M_\oplus$ for the resonant population, and $M = 11.75^{+5.7}_{-3.8}\ M_\oplus$ for the non-resonant population.

4.4. The resonant dynamics

Figure 4 shows the evolution of the Laplace angle over 50 years, obtained by integrating the best fit of the final posterior. The five inner planets of K2-138 form a chain of zero-order three-body resonances, which is the type of resonance found in other known resonant chains, defined by

$$k/P_n - (k+q)/P_{n+1} + q/P_{n+2} \sim 0, \tag{6}$$

with k and q integers. The associated resonant angles are defined as

$$\Psi_n = k\lambda_n - (k+q)\lambda_{n+1} + q\lambda_{n+2}. \tag{7}$$

For the three inner triplets of K2-138, $k = 2$ and $q = 3$. The outermost planet, K2-138 g, was initially thought to not be part of the chain, since the e, f, g triplet does not satisfy Eq. (7). However, Cerioni & Beaugé (2023) showed that the periods of the outer triplet is consistent with a first-order three-body resonance, which has not yet been confirmed in any exo-planetary systems. Unlike the condition to be in zero-order three-body resonance, which only depends on the period of the planets, the confirmation of first-order three-body resonance requires one to constrain the evolution of the longitude of pericenter of the planets, which can be obtained by seeing the effect of the first-order three-body resonance on the TTVs.

To probe the dynamical behavior associated with the proposed three-body resonance configuration, we began by computing a 2D stability map in the (P_g, e_g) plane, whereby we varied the orbital period and eccentricity of planet g, while keeping all other orbital elements and planetary masses fixed to the values listed in Tables 2 and 3. Since the mass of planet g is not well constrained by TTVs, we adopted a mass of 5 $M_\oplus$. For each grid point, the system was integrated over 5×10^4 years, and the stability was evaluated using frequency analysis criterion of Laskar (1990, 1993), following the approach of Correia et al. (2010); Couetdic et al. (2010). The stability indicator is presented as a colour index, with red zones representing strongly chaotic trajectories and dark blue zones indicating stable, quasi-periodic solutions. The resulting map (top panel of Fig. 5) displays a characteristic V-shaped structure, typical of two-body and three-body mean motion resonances, and in this case associated with the three-body commensurability between planets e, f, and g.

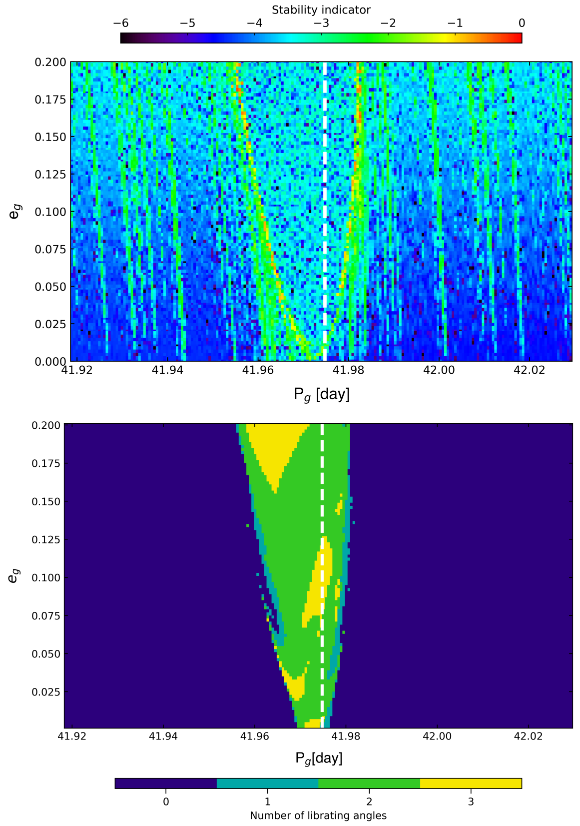

Fig. 5. Exploration of P_g and e_g. Top panel: Stability map of the K2-138 system in the (P_g, e_g) plane, obtained by varying the orbital period and eccentricity of planet g. All other orbital elements and planetary masses are fixed to the values in Tables 2 and 3, whereas the mass of planet g is fixed to $5\,M_\oplus$. For each initial condition, the system was integrated over 5×10^4 years, and a stability index was computed using frequency analysis of the mean longitude. Chaotic diffusion was measured by the variation in these frequencies. The colour scale shows the logarithmic variation of the stability index, with red indicating chaotic solutions, while the dark blue regions can be assumed to be stable on a billion-year timescale. Bottom panel: Number of librating angles, Ψ_i. The dashed white line in both panels shows the observed orbital period of planet g reported in Table 3.

We find that the orbital period of planet g places the system within this resonant structure, for eccentricities above $e_g \sim 0.01$. However, since the orbital parameters and mass of planet g are poorly constrained, this configuration remains tentative.

On the same grid, we also tracked the evolution of the three resonant angles

$$\psi_k = 2\lambda_e - 4\lambda_f + 3\lambda_g - \varpi_k, \quad \text{for } k = e, f, g \tag{8}$$

over the first 400 yr of each integration, and identified whether each angle librates or not. The number of librating angles is shown in the bottom panel of Fig. 5, which shows a complementary aspect of the dynamics in the (P_g, e_g) plane. From this figure, we can distinguish a V-shaped structure similar to that identified in the stability map (top panel of Fig. 5). Outside this region, all angles circulate, while inside at least one resonant angle librates, with most configurations showing two or three librating angles.

Additionally, we computed a 2D stability map in the (e_g, ϖ_g) plane, varying the eccentricity and longitude of pericenter of planet g, while keeping all other orbital elements and planetary masses fixed to the values listed in Tables 2 and 3, and the mass of planet g set to $5\,M_\oplus$. The aim is to assess whether dynamical arguments can help constrain these two currently unknown parameters. Figure 6 shows that the system can remain stable at low eccentricities only near $\varpi_g \sim 90°$, whereas for other values of ϖ_g, stability requires moderate to high eccentricities.

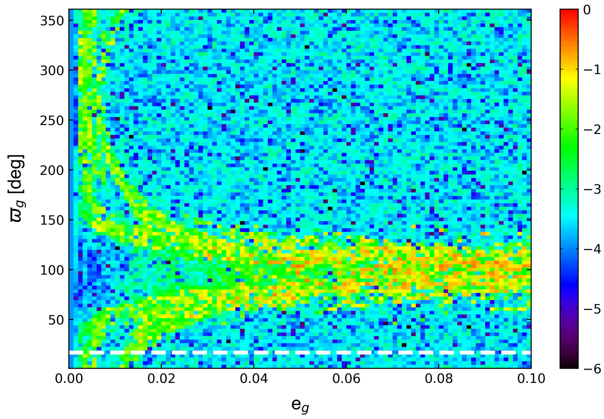

Fig. 6. Stability map of the K2-138 system in the $(e.g., \varpi_g)$ plane. The phase space is explored by varying these two parameters. All other orbital elements and planetary masses are fixed to the values in Tables 2 and 3, whereas the mass of planet g is fixed to $5\,M_\oplus$. As in Fig. 5, red zones corresponds to highly unstable orbits, while the dark blue regions can be assumed to be stable. The dashed white line shows the longitude of pericenter of planet g reported in Table 3. This stability map was computed by fixing the other parameter to the maximum likelihood value of the 'high-mass' posterior to illustrate the relative size of the first-order three-body resonance. The exact map can vary within the posterior, since some of the parameters, such as the longitude of pericenters of planet f, are poorly constrained.

This results in the difference in behaviour seen between the 'high-mass' and 'default' posteriors for planet g (Fig. 1). The default posterior shows flat TTVs, with a small eccentricity ($e_g \sim 0.001$), which is outside the resonance. The high-mass posterior shows the 40 minutes peak-to-peak TTVs amplitude, which is due to the libration in the resonance. For the 'high-mass' fit, we obtained $e_g \sim 0.3$. We note, however, that this value might be biased by the relatively low number of transits observed for planet g. Indeed, for K2-19, it has been shown that a relatively low number of transits coupled with outliers could lead to artificially large eccentricities (Almenara et al. 2025). As is shown in Figures 5 and 6, a wide range of values of e_g are possible for the system to be in the resonance. Fifteen photo-dynamical analyses were started at different points of the map shown in Fig. 6, and converged towards different values of eccentricity that could explain the observed data similarly well. We noticed that larger values of e_g correlated positively with the larger amplitude of TTVs for planet g, and with the larger radius of that planet. Transit depths of g similar to those published by Hardegree-Ullman et al. (2021) were only found with a solution with large eccentricity, and peak-to-peak TTVs of 10 minutes or more were only found when $e_g > 0.1$. The depth discrepancy could have three origins: the eccentricity of g could be quite large; we did not manage to find the correct solution for planet g at lower eccentricities; or a seventh planet is at the origin of TTVs on g. Additional data are required to draw a conclusion.

5. Summary and conclusion

Thanks to the extensive follow-up of K2-138, we were able to estimate the mass of the planets independently with RVs and photo-dynamics. We show that the photo-dynamical analysis is able to retrieve robust masses (with a low dependency on the chosen set of priors) for planets b to f. The RV and photo-dynamical masses are in good agreement for planets b to e, for which the photo-dynamical masses are robust to the choice of prior, and the RV masses are robust to the choice of activity model. The agreement breaks for the planets that are not robust in RVs (planets f and g) and in the photo-dynamical analysis (planet g). This makes K2-138 an ideal laboratory for testing mass robustness criteria for the two techniques, although it might not be possible to achieve a good understanding of the effect of stellar activity near the rotation harmonics until we acquire enough data to separate planet f (P=12.76 days) from the harmonic of the stellar rotation period at ~24 days (Lopez et al. 2019).

The joint analysis of photometric and RV data provides a slight improvement from the photo-dynamical fit by improving the precision of planets b to f. Thanks to the intensive follow-up effort, the five inner planets of K2-138 are characterized with a level of precision similar to TOI-178 or Kepler-60, with mass precision in the 5-10% range for planets b to e, and ~20% precision for planet f. The obtained masses and radius for planets b to f are similar to other sub-Neptunes in resonant chains (see Fig. 3). Fitting two distinct mass-radius relationships for resonant sub-Neptunes and non-resonant planets, we expanded on the results of Leleu et al. (2024a): (1) resonant sub-Neptunes, as a population, are puffier than non-resonant planets, and (2) the currently available constraints on these sub-populations point towards an inter-system uniformity of the mass-radius relation for resonant sub-Neptunes, possibly implying similarities in composition.

We were able to show that the inner five planets are indeed librating inside the Laplace resonant chain, but it remains unclear if the outermost planets, g, exhibit significant TTVs, and if these TTVs would be due to the first-order three-body resonance or an additional planet. Nonetheless, our dynamical analysis shows that the first-order three-body resonance occupies a large area of the phase space for the observed value of the period of planet g, but more data are required to fully confirm this configuration. As for TOI-178, the innermost Laplace angle is the one with the largest libration amplitude, which might be due to the tidal evolution of the system (Leleu et al. 2024b). We also note that, unlike other chains, the impact parameters of K2-138 are not fully compatible with 0 mutual inclination between the planet, with the innermost planet being the most inclined. This could be due to the oblateness of the star in the early stage of the evolution of the system. Overall, these new constraints will allow for a better comparison with models of formation and evolution of planetary systems (e.g. Emsenhuber et al. 2021; Izidoro et al. 2022).

Data availability

The detrended photometric data, the MCMC samples of the photo-dynamical and combined photo-dynamical and radial velocity analysis; and a list of transit times for planets b to f can be found on DACE: `https://dace.unige.ch/openData/?record=10.82180/dace-k2-138`.

References

Agol, E., & Deck, K. 2016, TTVFaster: First order eccentricity transit timing variations (TTVs), Astrophysics Source Code Library [record ascl:1604.012]
Agol, E., Dorn, C., Grimm, S. L., et al. 2020, arXiv e-prints [arXiv:2010.01074]
Ahrer, E., Queloz, D., Rajpaul, V. M., et al. 2021, MNRAS, 503, 1248
Allard, F. 2014, in Exploring the Formation and Evolution of Planetary Systems, 299, eds. M. Booth, B. C. Matthews, & J. R. Graham, 271
Almenara, J. M., Mardling, R., Leleu, A., et al. 2025, A&A, 703, A167
Beard, C., Robertson, P., Dai, F., et al. 2024, AJ, 167, 70
Benz, W., Broeg, C., Fortier, A., et al. 2021, Exp. Astron., 51, 109
Biersteker, J. B., & Schlichting, H. E. 2019, MNRAS, 485, 4454
Blackwell, D. E., & Shallis, M. J. 1977, MNRAS, 180, 177
Bonfanti, A., Ortolani, S., Piotto, G., & Nascimbeni, V. 2015, A&A, 575, A18
Bonfanti, A., Ortolani, S., & Nascimbeni, V. 2016, A&A, 585, A5
Bonfanti, A., Delrez, L., Hooton, M. J., et al. 2021, A&A, 646, A157
Bonfils, X., Astudillo-Defru, N., Díaz, R., et al. 2018, A&A, 613, A25
Boué, G., Oshagh, M., Montalto, M., & Santos, N. C. 2012, MNRAS, 422, L57
Brandeker, A., Heng, K., Lendl, M., et al. 2022, A&A, 659, L4
Carter, J. A., Agol, E., Chaplin, W. J., et al. 2012, Science, 337, 556
Castelli, F., & Kurucz, R. L. 2003, in IAU Symposium, 210, Modelling of Stellar Atmospheres, eds. N. Piskunov, W. W. Weiss, & D. F. Gray, A20
Cerioni, M., & Beaugé, C. 2023, ApJ, 954, 57
Christiansen, J. L., Crossfield, I. J. M., Barentsen, G., et al. 2018, AJ, 155, 57
Correia, A. C. M., Couetdic, J., Laskar, J., et al. 2010, A&A, 511, A21
Cossou, C., Raymond, S. N., Hersant, F., & Pierens, A. 2014, A&A, 569, A56
Couetdic, J., Laskar, J., Correia, A. C. M., Mayor, M., & Udry, S. 2010, A&A, 519, A10
Dai, F., Masuda, K., Beard, C., et al. 2023, AJ, 165, 33
Deck, K. M., & Agol, E. 2016, ApJ, 821, 96
Deck, K. M., Agol, E., Holman, M. J., & Nesvorný, D. 2014, ApJ, 787, 132
Deline, A., Hooton, M. J., Lendl, M., et al. 2022, A&A, 659, A74
Delisle, J. B., Hara, N., & Ségransan, D. 2020, A&A, 638, A95
Dumusque, X., Cretignier, M., Sosnowska, D., et al. 2021, A&A, 648, A103
Emsenhuber, A., Mordasini, C., Burn, R., et al. 2021, A&A, 656, A69
Fressin, F., Torres, G., Charbonneau, D., et al. 2013, ApJ, 766, 81
Gaia Collaboration (Brown, A. G. A., et al.) 2021, A&A, 649, A1
Gaia Collaboration (Vallenari, A., et al.) 2023, A&A, 674, A1
Gillon, M., Triaud, A. H. M. J., Demory, B.-O., et al. 2017, Nature, 542, 456
Goldreich, P., & Tremaine, S. 1979, ApJ, 233, 857
Goździewski, K., Migaszewski, C., Panichi, F., & Szuszkiewicz, E. 2016, MNRAS, 455, L104
Hadden, S., & Lithwick, Y. 2017, AJ, 154, 5
Hara, N. C., & Delisle, J.-B. 2025, A&A, 696, A141
Hara, N. C., Boué, G., Laskar, J., Delisle, J. B., & Unger, N. 2019, MNRAS, 489, 738
Hardegree-Ullman, K. K., Christiansen, J. L., Ciardi, D. R., et al. 2021, AJ, 161, 219
Howard, A. W., Marcy, G. W., Bryson, S. T., et al. 2012, ApJS, 201, 15
Howell, S. B., Sobeck, C., Haas, M., et al. 2014, PASP, 126, 398
Izidoro, A., Ogihara, M., Raymond, S. N., et al. 2017, MNRAS, 470, 1750
Izidoro, A., Schlichting, H. E., Isella, A., et al. 2022, ApJ, 939, L19
Jenkins, J. M., Twicken, J. D., McCauliff, S., et al. 2016, SPIE Conf. Ser., 9913, 99133E
Kipping, D. M. 2013, MNRAS, 434, L51
Korth, J., Chaturvedi, P., Parviainen, H., et al. 2024, ApJ, 971, L28
Kreidberg, L. 2015, PASP, 127, 1161
Kurucz, R. L. 1993, SYNTHE spectrum synthesis programs and line data
Laskar, J. 1990, Icarus, 88, 266
Laskar, J. 1993, Physica D: Nonlinear Phenomena, 67, 257
Lee, E. J., & Chiang, E. 2016, ApJ, 817, 90
Leleu, A., Alibert, Y., Hara, N. C., et al. 2021a, A&A, 649, A26
Leleu, A., Chatel, G., Udry, S., et al. 2021b, A&A, 655, A66
Leleu, A., Delisle, J. B., Udry, S., et al. 2023, A&A, 669, A117
Leleu, A., Delisle, J. B., Burn, R., et al. 2024a A&A, 687, L1
Leleu, A., Delisle, J. B., Delrez, L., et al. 2024b, A&A, 688, A211
Lindegren, L., Bastian, U., Biermann, M., et al. 2021, A&A, 649, A4
Lithwick, Y., Xie, J., & Wu, Y. 2012, ApJ, 761, 122
Lopez, T. A., Barros, S. C. C., Santerne, A., et al. 2019, A&A, 631, A90
Lovis, C., Mayor, M., Bouchy, F., et al. 2009, in Transiting Planets, 253, eds. F. Pont, D. Sasselov, & M. J. Holman, 502
Luger, R., Sestovic, M., Kruse, E., et al. 2017, Nat. Astron., 1, 0129
Luque, R., Osborn, H. P., Leleu, A., et al. 2023, Nature, 623, 932
MacDonald, M. G., Ragozzine, D., Fabrycky, D. C., et al. 2016, AJ, 152, 105
Marigo, P., Girardi, L., Bressan, A., et al. 2017, ApJ, 835, 77
Masset, F. S., Morbidelli, A., Crida, A., & Ferreira, J. 2006, ApJ, 642, 478
Masuda, K., & Tamayo, D. 2020, AJ, 160, 224
Mayor, M., Pepe, F., Queloz, D., et al. 2003, The Messenger, 114, 20
Millholland, S. 2019, ApJ, 886, 72
Millholland, S. C., Lara, T., & Toomlaid, J. 2024, ApJ, 961, 203
Mills, S. M., Fabrycky, D. C., Migaszewski, C., et al. 2016, Nature, 533, 509
Nesvorný, D., & Vokrouhlický, D. 2016, ApJ, 823, 72
Ogihara, M., & Ida, S. 2009, ApJ, 699, 824

Ragozzine, D. & Holman, M. J. 2010, arXiv e-prints [arXiv:1006.3727]
Ricker, G. R., Winn, J. N., Vanderspek, R., et al. 2015, J. Astron. Telesc. Instrum. Syst., 1, 014003
Rivera, E. J., Laughlin, G., Butler, R. P., et al. 2010, ApJ, 719, 890
Salmon, S. J. A. J., Van Grootel, V., Buldgen, G., Dupret, M. A., & Eggenberger, P. 2021, A&A, 646, A7
Santos, N. C., Sousa, S. G., Mortier, A., et al. 2013, A&A, 556, A150
Schanche, N., Hébrard, G., Collier Cameron, A., et al. 2020, MNRAS, 499, 428
Scuflaire, R., Théado, S., Montalbán, J., et al. 2008, Ap&SS, 316, 83
Skrutskie, M. F., Cutri, R. M., Stiening, R., et al. 2006, AJ, 131, 1163
Smith, J. C., Stumpe, M. C., Van Cleve, J. E., et al. 2012, PASP, 124, 1000
Sneden, C. A. 1973, PhD thesis, The University of Texas at Austin
Sousa, S. G. 2014, in Determination of Atmospheric Parameters of B, eds. E. Niemczura, B. Smalley, & W. Pych, 297
Sousa, S. G., Santos, N. C., Mayor, M., et al. 2008, A&A, 487, 373
Sousa, S. G., Santos, N. C., Israelian, G., Mayor, M., & Monteiro, M. J. P. F. G. 2007, A&A, 469, 783
Sousa, S. G., Santos, N. C., Adibekyan, V., Delgado-Mena, E., & Israelian, G. 2015, A&A, 577, A67
Sousa, S. G., Adibekyan, V., Delgado-Mena, E., et al. 2021, A&A, 656, A53
Stumpe, M. C., Smith, J. C., Van Cleve, J. E., et al. 2012, PASP, 124, 985
Stumpe, M. C., Smith, J. C., Catanzarite, J. H., et al. 2014, PASP, 126, 100
Terquem, C., & Papaloizou, J. C. B. 2007, ApJ, 654, 1110
Vivien, H. G., Hoyer, S., Deleuil, M., et al. 2024, A&A, 688, A192
Weidenschilling, S. J., & Davis, D. R. 1985, Icarus, 62, 16
Werner, M. W., Roellig, T. L., Low, F. J., et al. 2004, ApJS, 154, 1
Wright, E. L., Eisenhardt, P. R. M., Mainzer, A. K., et al. 2010, AJ, 140, 1868

[1] Observatoire astronomique de l'Université de Genève, Chemin Pegasi 51, 1290 Versoix, Switzerland
[2] Space Research and Planetary Sciences, Physics Institute, University of Bern, Gesellschaftsstrasse 6, 3012 Bern, Switzerland
[3] IMCCE, UMR8028 CNRS, Observatoire de Paris, PSL Univ., Sorbonne Univ., 77 av. Denfert-Rochereau, 75014 Paris, France
[4] Department of Astronomy, Stockholm University, AlbaNova University Center, 10691 Stockholm, Sweden
[5] CFisUC, Departamento de Física, Universidade de Coimbra, 3004-516 Coimbra, Portugal
[6] Instituto de Astrofisica e Ciencias do Espaco, Universidade do Porto, CAUP, Rua das Estrelas, 4150-762 Porto, Portugal
[7] Departamento de Fisica e Astronomia, Faculdade de Ciencias, Universidade do Porto, Rua do Campo Alegre, 4169-007 Porto, Portugal
[8] Department of Physics, University of Warwick, Gibbet Hill Road, Coventry CV4 7AL, UK
[9] Center for Space and Habitability, University of Bern, Gesellschaftsstrasse 6, 3012 Bern, Switzerland
[10] Space Research Institute, Austrian Academy of Sciences, Schmiedlstrasse 6, 8042 Graz, Austria
[11] Space sciences, Technologies and Astrophysics Research (STAR) Institute, Université de Liège, Allée du 6 Août 19C, 4000 Liège, Belgium
[12] Instituto de Astrofísica de Canarias, Vía Láctea s/n, 38200 La Laguna, Tenerife, Spain
[13] Departamento de Astrofísica, Universidad de La Laguna, Astrofísico Francisco Sanchez s/n, 38206 La Laguna, Tenerife, Spain
[14] Admatis, 5. Kandó Kálmán Street, 3534 Miskolc, Hungary
[15] Depto. de Astrofísica, Centro de Astrobiología (CSIC-INTA), ESAC campus, 28692 Villanueva de la Cañada (Madrid), Spain
[16] INAF, Osservatorio Astronomico di Padova, Vicolo dell'Osservatorio 5, 35122 Padova, Italy
[17] Centre for Exoplanet Science, SUPA School of Physics and Astronomy, University of St Andrews, North Haugh, St Andrews KY16 9SS, UK
[18] European Space Agency (ESA), European Space Research and Technology Centre (ESTEC), Keplerlaan 1, 2201 AZ Noordwijk, The Netherlands
[19] Institute of Space Research, German Aerospace Center (DLR), Rutherfordstrasse 2, 12489 Berlin, Germany
[20] INAF, Osservatorio Astrofisico di Torino, Via Osservatorio, 20, 10025 Pino Torinese To, Italy
[21] Centre for Mathematical Sciences, Lund University, Box 118, 221 00 Lund, Sweden
[22] Aix Marseille Univ, CNRS, CNES, LAM, 38 rue Frédéric Joliot-Curie, 13388 Marseille, France
[23] ARTORG Center for Biomedical Engineering Research, University of Bern, Bern, Switzerland
[24] ELTE Gothard Astrophysical Observatory, 9700 Szombathely, Szent Imre h. u. 112, Hungary
[25] SRON Netherlands Institute for Space Research, Niels Bohrweg 4, 2333 CA Leiden, The Netherlands
[26] Centre Vie dans l'Univers, Faculté des sciences, Université de Genève, Quai Ernest-Ansermet 30, 1211 Genève 4, Switzerland
[27] Leiden Observatory, University of Leiden, PO Box 9513, 2300 RA Leiden, The Netherlands
[28] Department of Space, Earth and Environment, Chalmers University of Technology, Onsala Space Observatory, 439 92 Onsala, Sweden
[29] Dipartimento di Fisica, Università degli Studi di Torino, via Pietro Giuria 1, 10125 Torino, Italy
[30] National and Kapodistrian University of Athens, Department of Physics, University Campus, Zografos, 157 84 Athens, Greece
[31] Astrobiology Research Unit, Université de Liège, Allée du 6 Août 19C, 4000 Liège, Belgium
[32] Department of Astrophysics, University of Vienna, Türkenschanzstrasse 17, 1180 Vienna, Austria
[33] Institute for Theoretical Physics and Computational Physics, Graz University of Technology, Petersgasse 16, 8010 Graz, Austria
[34] Konkoly Observatory, Research Centre for Astronomy and Earth Sciences, 1121 Budapest, Konkoly Thege Miklós út 15–17, Hungary
[35] ELTE Eötvös Loránd University, Institute of Physics, Pázmány Péter sétány 1/A, 1117 Budapest, Hungary
[36] German Aerospace Center (DLR), Institute of Optical Sensor Systems, Rutherfordstraße 2, 12489 Berlin, Germany
[37] Institut d'astrophysique de Paris, UMR7095 CNRS, Université Pierre & Marie Curie, 98bis blvd. Arago, 75014 Paris, France
[38] Astrophysics Group, Lennard Jones Building, Keele University, Staffordshire ST5 5BG, UK
[39] European Space Agency, ESA – European Space Astronomy Centre, Camino Bajo del Castillo s/n, 28692 Villanueva de la Cañada, Madrid, Spain
[40] ETH Zurich, Department of Physics, Wolfgang-Pauli-Strasse 2, 8093 Zurich, Switzerland
[41] INAF, Osservatorio Astrofisico di Catania, Via S. Sofia 78, 95123 Catania, Italy
[42] Weltraumforschung und Planetologie, Physikalisches Institut, University of Bern, Gesellschaftsstrasse 6, 3012 Bern, Switzerland
[43] Dipartimento di Fisica e Astronomia "Galileo Galilei", Università degli Studi di Padova, Vicolo dell'Osservatorio 3, 35122 Padova, Italy
[44] Cavendish Laboratory, JJ Thomson Avenue, Cambridge CB3 0HE, UK
[45] German Aerospace Center (DLR), Markgrafenstrasse 37, 10117 Berlin, Germany
[46] Institut fuer Geologische Wissenschaften, Freie Universitaet Berlin, Malteserstrasse 74-100, 12249 Berlin, Germany
[47] Institut de Ciencies de l'Espai (ICE, CSIC), Campus UAB, Can Magrans s/n, 08193 Bellaterra, Spain
[48] Institut d'Estudis Espacials de Catalunya (IEEC), 08860 Castelldefels (Barcelona), Spain
[49] HUN-REN-ELTE Exoplanet Research Group, Szent Imre h. u. 112., Szombathely 9700, Hungary
[50] Leiden Observatory, University of Leiden, Einsteinweg 55, 2333 CA Leiden, The Netherlands
[51] Institute of Astronomy, University of Cambridge, Madingley Road, Cambridge CB3 0HA, UK

Appendix A: Acknowledgements

Acknowledgements. CHEOPS is an ESA mission in partnership with Switzerland with important contributions to the payload and the ground segment from Austria, Belgium, France, Germany, Hungary, Italy, Portugal, Spain, Sweden, and the United Kingdom. The CHEOPS Consortium would like to gratefully acknowledge the support received by all the agencies, offices, universities, and industries involved. Their flexibility and willingness to explore new approaches were essential to the success of this mission. CHEOPS data analysed in this article will be made available in the CHEOPS mission archive (https://cheops.unige.ch/archive_browser/). This work has been carried out within the framework of the NCCR PlanetS supported by the Swiss National Science Foundation under grants 51NF40_182901 and 51NF40_205606. AL acknowledges support of the Swiss National Science Foundation under grant number TMSGI2_211697. ABr was supported by the SNSA. ACMC acknowledges support from the FCT, Portugal, through the CFisUC projects UIDB/04564/2020 and UIDP/04564/2020, with DOI identifiers 10.54499/UIDB/04564/2020 and 10.54499/UIDP/04564/2020, respectively. A.C., A.D., B.E., K.G., and J.K. acknowledge their role as ESA-appointed CHEOPS Science Team Members. S.G.S. acknowledge support from FCT through FCT contract nr. CEECIND/00826/2018 and POPH/FSE (EC). The Portuguese team thanks the Portuguese Space Agency for the provision of financial support in the framework of the PRODEX Programme of the European Space Agency (ESA) under contract number 4000142255. TWi acknowledges support from the UKSA and the University of Warwick. CBr and ASi acknowledge support from the Swiss Space Office through the ESA PRODEX program. A.C., A.D., B.E., K.G., and J.K. acknowledge their role as ESA-appointed CHEOPS Science Team Members. The authors acknowledge support from the Swiss NCCR PlanetS and the Swiss National Science Foundation. This work has been carried out within the framework of the NCCR PlanetS supported by the Swiss National Science Foundation under grants 51NF40182901 and 51NF40205606. J.K. acknowledges support from the Swiss National Science Foundation under grant number TMSGI2_211697. BAk and MLe acknowledge support of the Swiss National Science Foundation under grant number PCEFP2_194576. YAl acknowledges support from the Swiss National Science Foundation (SNSF) under grant 200020_192038. RAl, DBa, EPa, IRi, and EVi acknowledge financial support from the Agencia Estatal de Investigación of the Ministerio de Ciencia e Innovación MCIN/AEI/10.13039/501100011033 and the ERDF "A way of making Europe" through projects PID2021-125627OB-C31, PID2021-125627OB-C32, PID2021-127289NB-I00, PID2023-150468NB-I00 and PID2023-149439NB-C41. SCCB acknowledges the support from Fundação para a Ciência e Tecnologia (FCT) in the form of work contract through the Scientific Employment Incentive program with reference 2023.06687.CEECIND and DOI 10.54499/2023.06687.CEECIND/CP2839/CT0002. LBo, VNa, IPa, GPi, RRa, and GSc acknowledge support from CHEOPS ASI-INAF agreement n. 2019-29-HH.0. ACC acknowledges support from STFC consolidated grant number ST/V000861/1, and UKSA grant number ST/X002217/1. P.E.C. is funded by the Austrian Science Fund (FWF) Erwin Schroedinger Fellowship, program J4595-N. This project was supported by the CNES. This work was supported by FCT – Fundação para a Ciência e a Tecnologia through national funds and by FEDER through COMPETE2020 through the research grants UIDB/04434/2020, UIDP/04434/2020, 2022.06962.PTDC. O.D.S.D. is supported in the form of work contract (DL 57/2016/CP1364/CT0004) funded by national funds through FCT. B.-O. D. acknowledges support from the Swiss State Secretariat for Education, Research and Innovation (SERI) under contract number MB22.00046. ADe, BEd, and KGa acknowledge their role as ESA-appointed CHEOPS Science Team Members. This project has received funding from the Swiss National Science Foundation for project 200021_200726. It has also been carried out within the framework of the National Centre of Competence in Research PlanetS supported by the Swiss National Science Foundation under grant 51NF40_205606. The authors acknowledge the financial support of the SNSF. MF and CMP gratefully acknowledge the support of the Swedish National Space Agency (DNR 65/19, 174/18). DG gratefully acknowledges financial support from the CRT foundation under Grant No. 2018.2323 "Gaseousor rocky? Unveiling the nature of small worlds". M.G. is an F.R.S.-FNRS Senior Research Associate. MNG is the ESA CHEOPS Project Scientist and Mission Representative. BMM is the ESA CHEOPS Project Scientist. KGI was the ESA CHEOPS Project Scientist until the end of December 2022 and Mission Representative until the end of January 2023. All of them are/were responsible for the Guest Observers (GO) Programme. None of them relay/relayed proprietary information between the GO and Guaranteed Time Observation (GTO) Programmes, nor do/did they decide on the definition and target selection of the GTO Programme. CHe acknowledges financial support from the Österreichische Akademie 1158 der Wissenschaften and from the European Union H2020-MSCA-ITN-2019 1159 under Grant Agreement no. 860470 (CHAMELEON). Calculations were performed using supercomputer resources provided by the Vienna Scientific Cluster (VSC). K.W.F.L. was supported by Deutsche Forschungsgemeinschaft grants RA714/14-1 within the DFG Schwerpunkt SPP 1992, Exploring the Diversity of Extrasolar Planets. This work was granted access to the HPC resources of MesoPSL financed by the Region Ile de France and the project Equip@Meso (reference ANR-10-EQPX-29-01) of the programme Investissements d'Avenir supervised by the Agence Nationale pour la Recherche. PM acknowledges support from STFC research grant number ST/R000638/1. This work was also partially supported by a grant from the Simons Foundation (PI Queloz, grant number 327127). NCSa acknowledges funding by the European Union (ERC, FIERCE, 101052347). Views and opinions expressed are however those of the author(s) only and do not necessarily reflect those of the European Union or the European Research Council. Neither the European Union nor the granting authority can be held responsible for them. GyMSz acknowledges the support of the Hungarian National Research, Development and Innovation Office (NKFIH) grant K-125015, a a PRODEX Experiment Agreement No. 4000137122, the Lendulet LP2018-7/2021 grant of the Hungarian Academy of Science and the support of the city of Szombathely. V.V.G. is an F.R.S-FNRS Research Associate. JV acknowledges support from the Swiss National Science Foundation (SNSF) under grant PZ00P2_208945. NAW acknowledges UKSA grant ST/R004838/1.

Appendix B: Detrended photometry

Appendix C: Robustness of the RV mass estimation and activity modelling

Table C.1. Masses posterior of the RV analysis with the final set of priors shown in Fig. 2.

$m_b[M_{Earth}]$	$4.17^{+1.35}_{-1.69}$
$m_c[M_{Earth}]$	$4.86^{+1.86}_{-1.83}$
$m_d[M_{Earth}]$	$6.06^{+2.29}_{-1.88}$
$m_e[M_{Earth}]$	$10.64^{+2.07}_{-2.65}$
$m_f[M_{Earth}]$	$0.37^{+1.12}_{-0.30}$
$m_g[M_{Earth}]$	$0.41^{+2.21}_{-0.33}$

Notes. The associated noise model is given in the left column of Table D.2.

Poorly modelled noise sources can introduce biases, in particular in parameters which are always positive such as mass and eccentricity (Hara et al. 2019). We performed a similar analysis as for TOI-178 (see Leleu et al. 2024b, Appendix D), un order to test the robustness of the mass estimates of the planets obtained from the HARPS RVs. We analyzed the RV time series using different activity models and different mass priors. The results are shown in Fig. C.1. In all cases, we fixed the periods and phases of the planets to the values of Lopez et al. (2019, median values from Table A.4). We assumed circular orbits and only let the semi-amplitudes of the RV signals to vary. We tested each activity model with a log-uniform *default* prior on the semi-amplitudes and with a uniform *high-mass* prior. In the case of the high-mass prior, we also allow for negative semi-amplitudes (hence negative planetary masses). A negative semi-amplitude means that the signal is found in opposite phase with what is expected from the transit. We allow for this to better assess the reliability of the mass constraints we get from RVs and the dependency of the results with respect to the activity model and the mass prior. We used the `spleaf` GP package (Delisle et al. 2020), with different FENRIR data-driven kernels (Hara & Delisle 2025). The GP is trained simultaneously on the RVs and two indicators among the FWHM, contrast, and bisector-span (bispan). We included from 1 to 3 harmonics of the rotation period in the single-mode FENRIR kernel, with a Matérn 1/2 decay envelope. We additionally always included a single-mode short decay term (Matérn 1/2 kernel) to model (super)-granulation. From Fig. C.1, we conclude that the mass of the four inner planets seems robust to changes in the

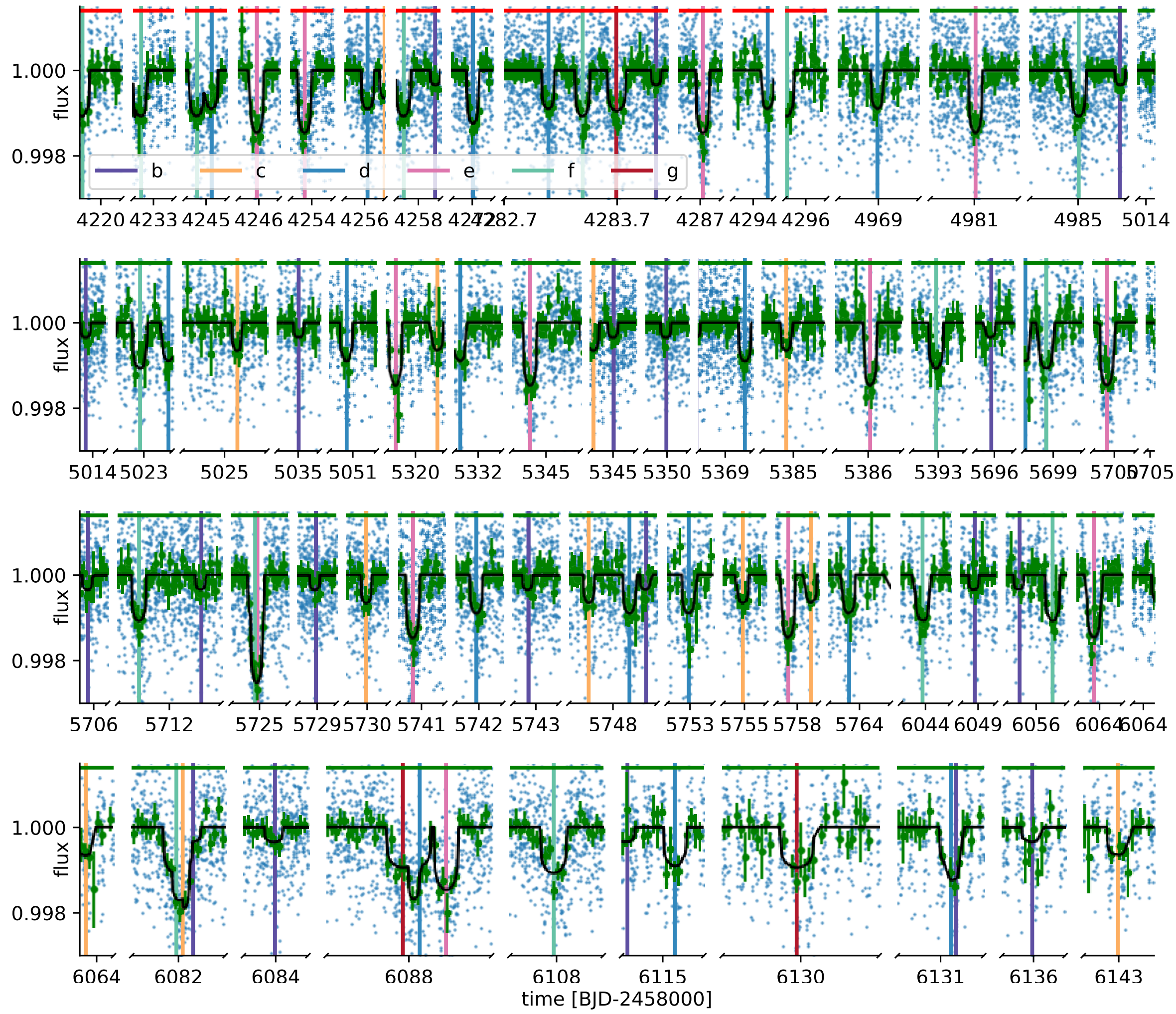

Fig. B.1. Detrended photometry of CHEOPS. The blue dots are the measured points, the green error bars are the binned points. The vertical coloured lines show the position of the transits of each planet. The red upper lines show the transit that were first published in Vivien et al. (2024). The green upper line show the transits that are published in this study.

activity model and in the mass prior. As in the case of TOI-178 (Leleu et al. 2024b), the masses of the outer planets (f at about 12.8 d and g at about 42 d), which are closer to the rotation period (about 24 d) are both prior and activity model dependent.

To avoid biasing the final mass estimates for the combined RV + photodynamical fit, but to still benefit from the RV constraints, we selected from this analysis the two-harmonics model trained on FWHM and contrast. Indeed, for the most model-sensitive planets (f, and g) this model exhibits large uncertainties on the mass posteriors and strong prior-sensitivity which reflects well the overall lack of constraint we have on these masses. The RV, FWHM and contrast and the 1-sigma interval of the model is shown in Fig. C.2 However, this does not mean that this an intrinsically better model for stellar activity. We stress out here the need for additional high-precision RV measurements to better constrain the masses and activity model.

Appendix D: Posteriors of stellar and noise parameters

The posteriors of the stellar and noise parameters are given in Tables D.1 and D.2.

Appendix E: Fitting mass-radius relations

To estimate a mass-radius relation for both the resonant chain population and the non-resonant population, we look for the conditional distribution of the mass of a planet given its radius: $p(M|R)$. We assume this conditional distribution to be a log-normal distribution centered on $m = ar + b$, with $m = \log M$ and $r = \log R$, respectively. with a standard deviation σ, and we aim at constraining the parameters $\theta = (a, b, \sigma)$ of this law.

We have noisy measurements of the mass and radius of some planets. Let $x_i = \begin{pmatrix} m_i \\ r_i \end{pmatrix}$ be the vector of log-mass and log-radius measurements for planet i. We assume Gaussian uncertainties and no correlation between these measurements such that the covariance matrix of x_i is $\Sigma_i = \begin{pmatrix} \sigma_{m_i}^2 & 0 \\ 0 & \sigma_{r_i}^2 \end{pmatrix}$.

To compute the likelihood $p(x_i|\theta)$, we first needed to assume a distribution of radii in the population. We assumed it to be log-uniform over a wide interval, or equivalently to be log-normal with a large standard deviation σ'. We looked for the asymptotic behavior for $\sigma' \to +\infty$. We performed a change of coordinates:

$$y = Ax + B, \tag{E.1}$$

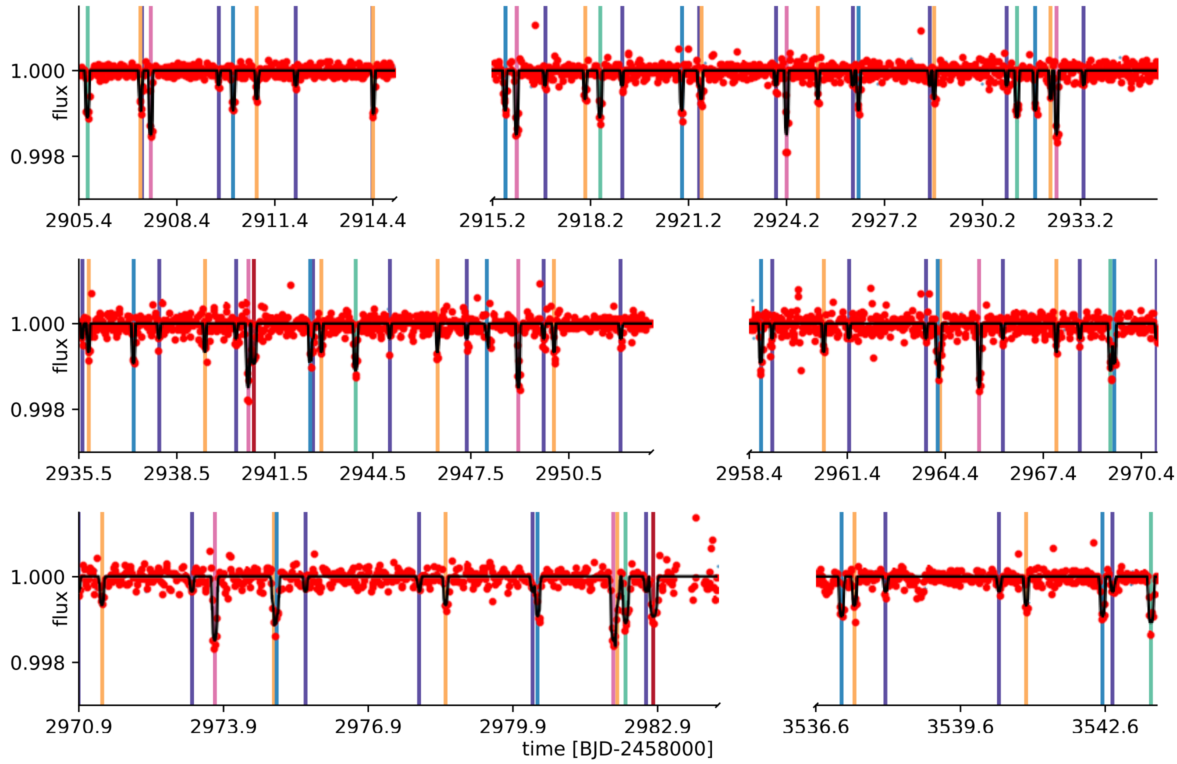

Fig. B.2. Detrended photometry of K2. The red error bars are the measured points. The vertical coloured lines show the position of transit of each planet; see Fig. B.1.

Table D.1. Fitted properties of the star and noise parameters.

Parameter	Prior	photo-dynamical	photo-dynamical + RV
		Star	
$\rho_\star$ [$\rho_\odot$]	$\mathcal{N}$(1.43,0.09)	$1.477^{+0.066}_{-0.062}$	$1.492^{+0.052}_{-0.071}$
$R_\star$ [$R_\odot$]	$\mathcal{N}$(0.84,0.01)	$0.8454^{+0.0068}_{-0.0050}$	$0.8457^{+0.0063}_{-0.0054}$
		TESS	
σ	$\mathcal{U}$(0.0e+00,1.0e+30)	$3.6e-05^{+3.3e-05}_{-2.7e-05}$	$3.7e-05^{+3.2e-05}_{-2.5e-05}$
$u1$	$\mathcal{N}$(0.40,0.04)	$0.402^{+0.046}_{-0.034}$	$0.407^{+0.035}_{-0.038}$
$u2$	$\mathcal{N}$(0.20,0.02)	$0.205^{+0.019}_{-0.019}$	$0.205^{+0.017}_{-0.017}$
		CHEOPS	
σ	$\mathcal{U}$(0.0e+00,1.0e+30)	$5.2e-04^{+8.6e-06}_{-8.0e-06}$	$5.2e-04^{+7.2e-06}_{-7.9e-06}$
$u1$	$\mathcal{N}$(0.39,0.02)	$0.399^{+0.016}_{-0.019}$	$0.398^{+0.014}_{-0.014}$
$u2$	$\mathcal{N}$(0.23,0.03)	$0.236^{+0.023}_{-0.025}$	$0.238^{+0.026}_{-0.022}$
		K2	
σ	$\mathcal{U}$(0.0e+00,1.0e+30)	$2.1e-04^{+2.8e-06}_{-2.7e-06}$	$2.1e-04^{+2.4e-06}_{-2.1e-06}$
$u1$	$\mathcal{N}$(0.50,0.01)	$0.4960^{+0.0099}_{-0.0077}$	$0.4966^{+0.0083}_{-0.0079}$
$u2$	$\mathcal{N}$(0.20,0.01)	$0.2053^{+0.0061}_{-0.0063}$	$0.2055^{+0.0053}_{-0.0069}$

Notes. Stellar and noise parameters, with σ the jitter terms and uk the limb-darkening coefficients.

with

$$A = \begin{pmatrix} 1 & -a \\ 0 & 1 \end{pmatrix} \tag{E.2}$$

$$B = -\begin{pmatrix} b \\ 0 \end{pmatrix}, \tag{E.3}$$

such that the first coordinate measures the distance from the linear law:

$$y_1 = d = m - ar - b, \tag{E.4}$$

while the second one is still $y_2 = r$. Our assumptions for the distribution of r and m in the population of planets are equivalent to assuming $y \sim \mathcal{N}(0, C_y)$, with $C_y = \begin{pmatrix} \sigma^2 & 0 \\ 0 & \sigma'^2 \end{pmatrix}$. The likelihood can be rewritten in terms of the new coordinates:

$$p(x_i|\theta) = \left|\frac{\partial y}{\partial x}\right| p(y_i|\theta) = |A|\, p(y_i|\theta) = p(y_i|\theta). \tag{E.5}$$

We denote by $y_{i,\mathrm{true}}$ the true value of y for planet i, while y_i is the measured value. We have $y_i = (y_i - y_{i,\mathrm{true}}) + y_{i,\mathrm{true}}$. The first

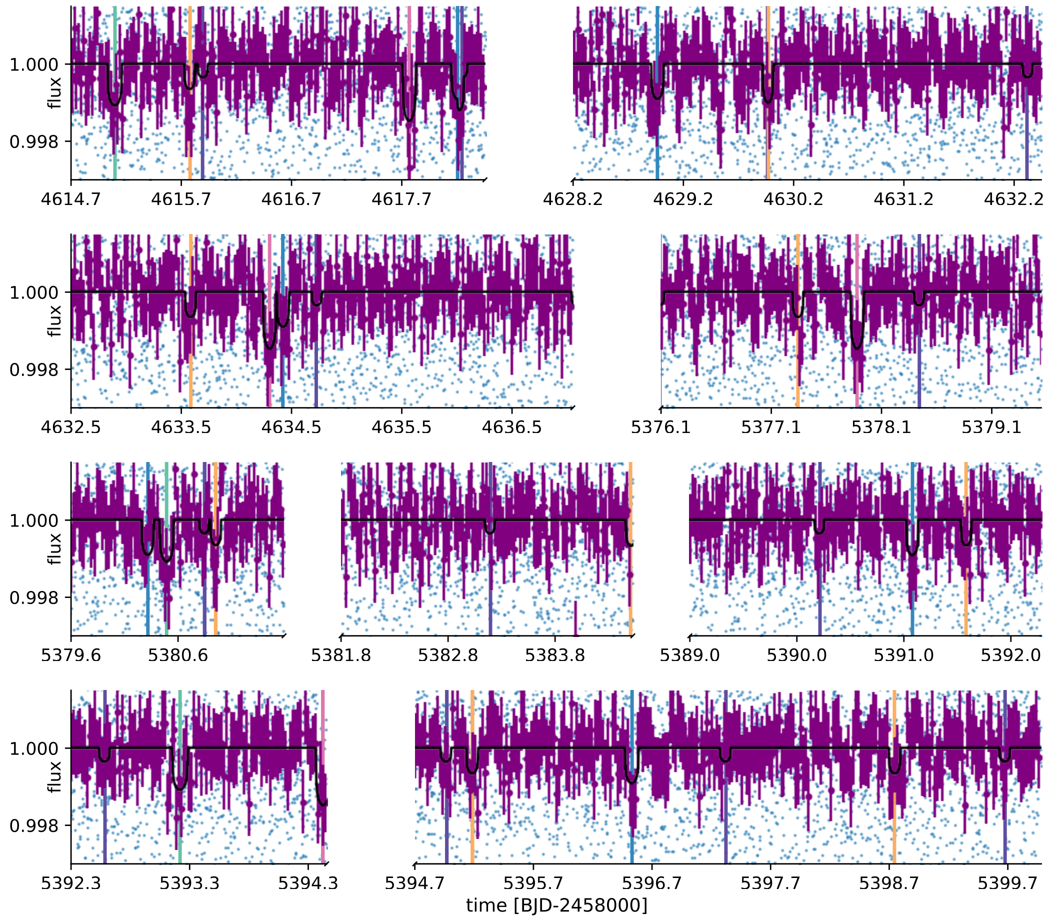

Fig. B.3. Detrended photometry of TESS. The blue dots are the measured point, the purple error bars are the binned points. The vertical coloured lines show the position of the transits of each planet; see Fig. B.1.

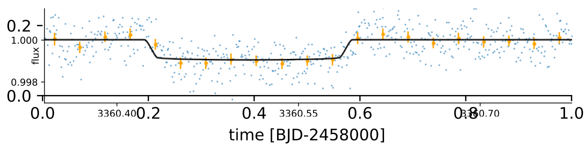

Fig. B.4. Detrended photometry of Spitzer. The blue dots are the measured point, the orange error bars are the binned points. The vertical coloured lines show the position of the transits of each planet; see Fig. B.1.

term $y_i - y_{i,\mathrm{true}} \sim \mathcal{N}(0, A\Sigma_i A^T)$ is the measurement error. The second term $y_{i,\mathrm{true}}$ follows the population distribution $\mathcal{N}(0, C_y)$ according to our assumptions. Both components are independent so y_i follows a Gaussian distribution $\mathcal{N}(0, A\Sigma_i A^T + C_y)$, and the likelihood is thus

$$p(x_i|\theta) = \frac{1}{|2\pi(A\Sigma_i A^T + C_y)|^{1/2}} \exp\left(-\frac{1}{2} y_i^T (A\Sigma_i A^T + C_y)^{-1} y_i\right). \tag{E.6}$$

In the limit of large σ' (i.e. log-uniform distribution over a wide interval of radii in the population), this expression simplifies to

$$p(x_i|\theta) = \frac{1}{\sqrt{2\pi}\sigma'} \frac{1}{\sqrt{2\pi(\sigma_{d_i}^2 + \sigma^2)}} \exp\left(-\frac{1}{2}\frac{d_i^2}{\sigma_{d_i}^2 + \sigma^2}\right) + \mathrm{o}\left(\frac{1}{\sigma'}\right), \tag{E.7}$$

with σ_{d_i} the uncertainty on the measure of d_i:

$$\sigma_{d_i}^2 = \sigma_{m_i}^2 + a^2\sigma_{r_i}^2. \tag{E.8}$$

We then used this likelihood in an MCMC to explore the parameters θ. The constant $\sqrt{2\pi}\sigma'$ factor in the likelihood can be neglected as we are only interested in likelihood ratios. We thus used the following asymptotic likelihood:

$$p(x_i|\theta) \propto \frac{1}{\sqrt{2\pi(\sigma_{d_i}^2 + \sigma^2)}} \exp\left(-\frac{1}{2}\frac{d_i^2}{\sigma_{d_i}^2 + \sigma^2}\right). \tag{E.9}$$

The overall likelihood for n planets is then

$$p(x|\theta) = \prod_{i=1}^{n} p(x_i|\theta). \tag{E.10}$$

From the MCMC exploration, we get N samples $(\theta_i)_{i=1...N}$ following $p(\theta|x)$. The posterior conditional probability of the mass

Table D.2. Fitted properties of the star and noise parameters.

Parameter	Prior	RV	photo-dynamical + RV
offset $H\alpha$	$\mathcal{U}$(-1.0e+300,1.0e+300)	$0.2468^{+0.0080}_{-0.0075}$	$0.2434^{+0.0036}_{-0.0034}$
σ RV	$\mathcal{U}$(-1.0e+300,1.0e+300)	$1.57^{+0.74}_{-0.84}$	$1.40^{+0.91}_{-0.80}$
σ FWHM	$\mathcal{U}$(-1.0e+300,1.0e+300)	$9.89^{+0.87}_{-0.88}$	$9.99^{+1.11}_{-1.05}$
σ Hα	$\mathcal{U}$(0.0e+00,3.0e+01)	$0.00443^{+2.6e-04}_{-3.0e-04}$	$0.00436^{+2.9e-04}_{-3.3e-04}$
GP granulation α_{000}	$\mathcal{U}$(0.0e+00,3.0e+01)	$4.11^{+0.45}_{-0.56}$	$4.10^{+0.54}_{-0.51}$
GP granulation α_{010}	$\mathcal{U}$(0.0e+00,3.0e+01)	$2.85^{+1.22}_{-1.11}$	$2.34^{+1.30}_{-1.44}$
GP granulation α_{011}	$\mathcal{N}$(0.0e+00,2.0e+02)	$-3.90^{+2.82}_{-2.43}$	$-0.70^{+3.46}_{-3.98}$
GP granulation α_{020}	$\mathcal{N}$(0.0e+00,2.0e+02)	$-8.9e-04^{+4.3e-04}_{-3.7e-04}$	$-8.6e-04^{+5.4e-04}_{-6.0e-04}$
GP granulation α_{021}	$\mathcal{N}$(0.0e+00,2.0e+02)	$-0.00160^{+7.3e-04}_{-7.1e-04}$	$-8.0e-04^{+0.0026}_{-0.0015}$
GP rotation α_{000}	$\mathcal{N}$(0.0e+00,2.0e+02)	$28.28^{+8.84}_{-7.83}$	$7.08^{+2.67}_{-2.59}$
GP rotation α_{010}	$\mathcal{N}$(0.0e+00,2.0e+02)	$151.5^{+53.3}_{-34.3}$	$42.8^{+12.7}_{-13.2}$
GP rotation α_{020}	$\mathcal{N}$(0.0e+00,2.0e+02)	$0.034^{+0.013}_{-0.008}$	$0.0094^{+0.0035}_{-0.0033}$
GP rotation α_{100}	$\mathcal{N}$(0.0e+00,2.0e+02)	$11.0^{+15.3}_{-15.1}$	$-0.04^{+6.76}_{-6.60}$
GP rotation α_{110}	$\mathcal{N}$(0.0e+00,2.0e+02)	$-2.9^{+11.4}_{-9.1}$	$-0.70^{+5.30}_{-6.13}$
GP rotation β_{110}	$\mathcal{N}$(0.0e+00,2.0e+02)	$-2.6^{+8.3}_{-12.2}$	$-0.80^{+6.24}_{-6.21}$
GP rotation α_{120}	$\mathcal{N}$(0.0e+00,2.0e+02)	$-0.0013^{+0.0033}_{-0.0036}$	$-8.7e-05^{+0.0016}_{-0.0016}$
GP rotation β_{120}	$\mathcal{N}$(0.0e+00,2.0e+02)	$-0.0049^{+0.0060}_{-0.0049}$	$8.9e-05^{+0.0021}_{-0.0030}$
GP rotation α_{200}	$\mathcal{N}$(0.0e+00,2.0e+02)	$-3.55^{+8.85}_{-6.07}$	$-0.11^{+1.45}_{-1.74}$
GP rotation α_{210}	$\mathcal{N}$(0.0e+00,2.0e+02)	-25^{+129}_{-94}	$-9.2^{+23.1}_{-11.0}$
GP rotation β_{210}	$\mathcal{N}$(0.0e+00,2.0e+02)	$-12.0^{+81.8}_{-81.4}$	$5.9^{+13.5}_{-12.5}$
GP rotation α_{220}	$\mathcal{N}$(0.0e+00,2.0e+02)	$-0.002^{+0.033}_{-0.023}$	$-0.0030^{+0.0057}_{-0.0030}$
GP rotation β_{220}	$\mathcal{N}$(0.0e+00,2.0e+02)	$-0.006^{+0.029}_{-0.022}$	$0.0013^{+0.0043}_{-0.0045}$
GP rotation α_{300}	$\mathcal{N}$(0.0e+00,2.0e+02)	$2.01^{+6.02}_{-9.03}$	$-0.72^{+2.36}_{-2.89}$
GP rotation α_{310}	$\mathcal{N}$(0.0e+00,2.0e+02)	$-32.5^{+56.4}_{-56.7}$	$-4.5^{+12.3}_{-18.3}$
GP rotation β_{310}	$\mathcal{N}$(0.0e+00,2.0e+02)	$-2.6^{+82.7}_{-66.1}$	$11.5^{+19.4}_{-15.4}$
GP rotation α_{320}	$\mathcal{N}$(0.0e+00,2.0e+02)	$-0.008^{+0.015}_{-0.014}$	$-3.8e-04^{+0.0036}_{-0.0046}$
GP rotation β_{320}	$\mathcal{N}$(0.0e+00,2.0e+02)	$0.002^{+0.022}_{-0.018}$	$0.0029^{+0.0047}_{-0.0037}$
GP granulation ρ	$\mathcal{N}$(0.0e+00,2.0e+02)	$0.23^{+0.12}_{-0.08}$	$0.24^{+0.19}_{-0.09}$
GP rotation P	$\mathcal{N}$(0.0e+00,2.0e+02)	$56.78^{+0.92}_{-1.21}$	$55.94^{+1.85}_{-2.40}$
GP rotation ρ	$\mathcal{LU}$(0.10,10.00)	23509^{+10384}_{-8586}	523^{+176}_{-50}

Notes. Noise parameters for the RV fit. σ are the jitter term for the velocity and indicators. P is the period of the GP. ρ is the decay timescale. α_{klm} and β_{klm} are amplitudes of the cosine and sine terms in the spleaf.term.MultiFourierKernel (`https://obswww.unige.ch/~delisle/spleaf/doc/_autosummary/spleaf.term.MultiFourierKernel.html#spleaf.term.MultiFourierKernel`), respectively, with k the harmonic (f = k/P), l the timeseries, and m the mode.

of a planet given its radius is

$$p(m|r,x) = \int p(m|r,\theta)p(\theta|x)\mathrm{d}\theta \tag{E.11}$$

$$\approx \frac{1}{N}\sum_{i=1}^{N} p(m|r,\theta_i) \tag{E.12}$$

$$= \frac{1}{N}\sum_{i=1}^{N} \frac{1}{\sqrt{2\pi}\sigma_i}\exp\left(-\frac{1}{2}\left(\frac{m-a_ir-b_i}{\sigma_i}\right)^2\right). \tag{E.13}$$

In particular, the conditional expectation (mean) is

$$\mathbb{E}(m|r,x) = \int \mathbb{E}(m|r,\theta)p(\theta|x)\mathrm{d}\theta \tag{E.14}$$

$$\approx \frac{1}{N}\sum_{i=1}^{N} \mathbb{E}(m|r,\theta_i) \tag{E.15}$$

$$= \frac{1}{N}\sum_{i=1}^{N} a_ir + b_i \tag{E.16}$$

$$= \langle ar+b\rangle\,, \tag{E.17}$$

$$= \langle a\rangle\, r + \langle b\rangle\,, \tag{E.18}$$

where $\langle X\rangle$ is the average value of X over all MCMC samples. Similarly, the conditional variance is

$$\mathrm{var}(m|r,x) = \mathbb{E}(m^2|r,x) - \mathbb{E}(m|r,x)^2 \tag{E.19}$$

$$= \int \mathbb{E}(m^2|r,\theta)p(\theta|x)\mathrm{d}\theta - \mathbb{E}(m|r,x)^2 \tag{E.20}$$

$$\approx \frac{1}{N}\sum_{i=1}^{N} \mathbb{E}(m^2|r,\theta_i) - \langle ar+b\rangle^2 \tag{E.21}$$

$$= \left\langle\sigma^2\right\rangle + \left\langle(ar+b)^2\right\rangle - \langle ar+b\rangle^2\,, \tag{E.22}$$

$$= \left\langle\sigma^2\right\rangle + \mathrm{var}(ar+b), \tag{E.23}$$

where

$$\mathrm{var}(ar+b) = r^2\,\mathrm{var}(a) + 2r\,\mathrm{cov}(a,b) + \mathrm{var}(b) \tag{E.24}$$

is the variance of $ar+b$ over all MCMC samples.

Appendix F: CHEOPS log

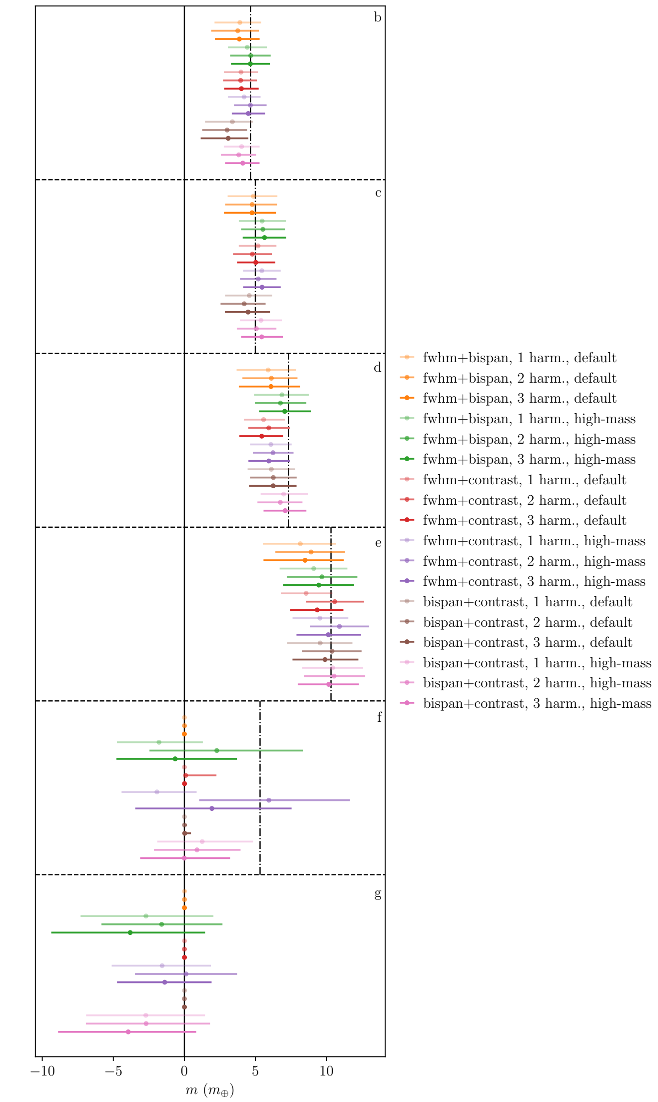

Fig. C.1. Comparison of RV mass estimates for various activity models and priors. The vertical dashed lines show the median of the TTV posterior.

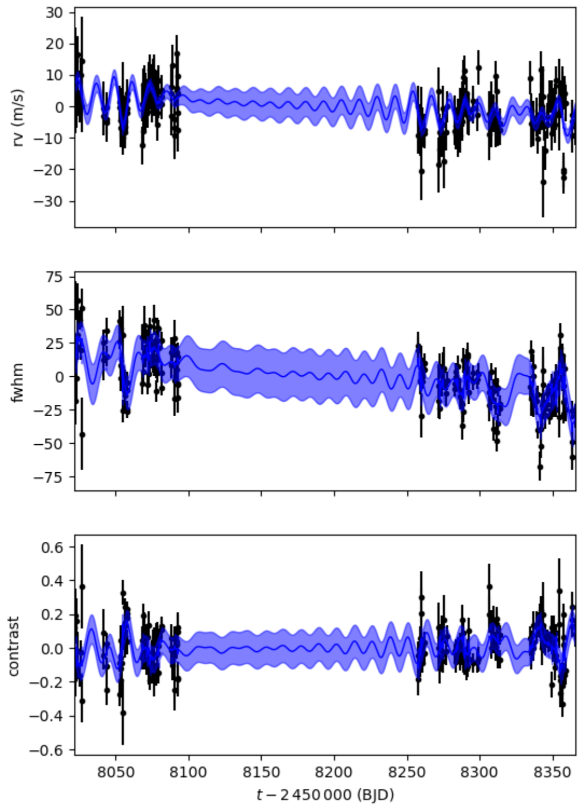

Fig. C.2. RV, FWHM, and contrast and the 1-sigma interval of the model chosen for the joint analysis.

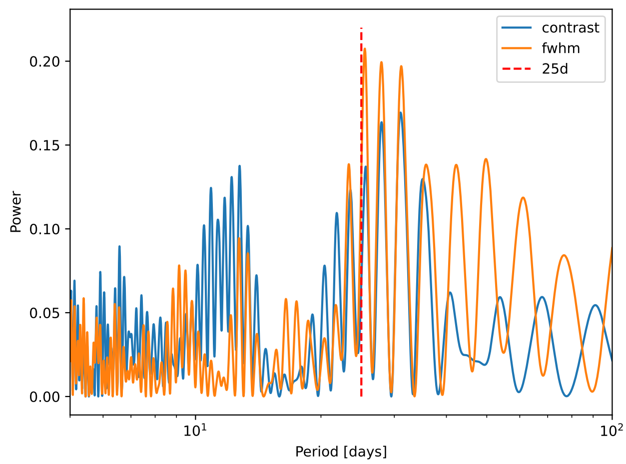

Fig. C.3. Periodogram of the contrast and FWHM and indicators that are used in the chosen model for the joint analysis. In both indicators, power can be seen near the stellar rotation period of $\sim$ 25 days. The strong oscillations in the periodogram are due to the sampling : the full 350 days baseline give a period resolution of $\Delta P = 1/(1/25 \pm 1/350) = [23.3, 26.9]$ at 25 days, explaining the narrow peaks, but the measurements are distributed in two chunks of $\sim$ 100 days each (see Fig. C.2), resulting in a much broader uncertainty of $\Delta P = 1/(1/25 \pm 100) = [20.0, 33.3]$, which is the envelop of the peaks in the 20-40 days range.

Table F.1. log of CHEOPS visits.

file_key	start date [BJD-2457000]	duration [hour]	reference
CH_PR210017_TG000301_V0300	2052.6223	8.90	Vivien et al. (2024)
CH_PR210017_TG000302_V0300	2065.3004	9.34	Vivien et al. (2024)
CH_PR210017_TG000303_V0300	2078.0530	9.10	Vivien et al. (2024)
CH_PR210017_TG000201_V0300	2078.8156	8.80	Vivien et al. (2024)
CH_PR210017_TG000202_V0300	2087.1186	8.99	Vivien et al. (2024)
CH_PR210017_TG000101_V0300	2088.8881	8.70	Vivien et al. (2024)
CH_PR210017_TG000304_V0300	2090.8478	9.39	Vivien et al. (2024)
CH_PR210017_TG000102_V0300	2105.1264	8.70	Vivien et al. (2024)
CH_PR210017_TG000501_V0300	2115.7352	34.73	Vivien et al. (2024)
CH_PR210017_TG000203_V0300	2120.0740	8.99	Vivien et al. (2024)
CH_PR210017_TG000103_V0300	2126.6307	8.70	Vivien et al. (2024)
CH_PR210017_TG000305_V0300	2129.1581	9.09	Vivien et al. (2024)
CH_PR120053_TG005601_V0300	2802.1297	17.26	this study
CH_PR120053_TG005501_V0300	2813.9086	18.71	this study
CH_PR120053_TG005401_V0300	2817.5823	20.54	this study
CH_PR120053_TG006501_V0300	2846.4294	8.94	this study
CH_PR120053_TG006801_V0300	2856.0652	12.16	this study
CH_PR120053_TG006401_V0300	2857.5970	18.01	this study
CH_PR120053_TG007001_V0300	2867.6146	9.02	this study
CH_PR120053_TG007201_V0300	2883.4114	10.00	this study
CH_PR140080_TG001401_V0300	3152.9657	12.36	this study
CH_PR140080_TG001402_V0300	3156.5312	9.20	this study
CH_PR140080_TG001501_V0300	3164.5900	10.01	this study
CH_PR140080_TG001601_V0300	3177.6731	14.64	this study
CH_PR140080_TG001301_V0300	3178.2974	9.62	this study
CH_PR140080_TG001302_V0300	3183.0267	9.10	this study
CH_PR140080_TG002901_V0300	3202.0587	11.39	this study
CH_PR140080_TG003401_V0300	3217.2487	13.49	this study
CH_PR140080_TG003001_V0300	3218.8312	14.74	this study
CH_PR140080_TG003301_V0300	3225.9934	11.29	this study
CH_PR140080_TG005801_V0300	3529.0469	8.32	this study
CH_PR140080_TG005401_V0300	3532.1560	12.57	this study
CH_PR140080_TG005501_V0300	3532.9776	9.52	this study
CH_PR140080_TG005802_V0300	3538.4515	8.22	this study
CH_PR140080_TG005402_V0300	3544.9253	22.09	this study
CH_PR140080_TG005403_V0300	3557.6560	12.16	this study
CH_PR140080_TG005803_V0300	3561.9817	8.10	this study
CH_PR140080_TG005901_V0300	3562.4900	8.90	this study
CH_PR140080_TG005502_V0300	3574.2829	9.92	this study
CH_PR140080_TG006001_V0300	3575.2246	10.19	this study
CH_PR140080_TG005804_V0300	3576.1232	9.77	this study
CH_PR140080_TG005902_V0300	3580.2856	18.72	this study
CH_PR140080_TG006002_V0300	3586.0347	9.75	this study
CH_PR140080_TG005903_V0300	3587.4034	9.14	this study
CH_PR140080_TG005503_V0300	3590.8233	9.20	this study
CH_PR140080_TG006003_V0300	3596.8522	13.32	this study
CH_PR140080_TG011801_V0300	3876.5896	10.64	this study
CH_PR140080_TG012201_V0300	3882.0615	7.50	this study
CH_PR140080_TG012202_V0300	3889.1251	12.94	this study
CH_PR140080_TG011901_V0300	3896.4782	9.75	this study
CH_PR140080_TG012101_V0300	3897.0512	8.75	this study
CH_PR140080_TG012801_V0300	3914.8330	10.97	this study
CH_PR140080_TG012401_V0300	3917.3317	7.57	this study
CH_PR140080_TG012901_V0300	3920.8343	19.41	this study
CH_PR140080_TG012802_V0300	3940.3468	10.97	this study
CH_PR140080_TG012601_V0300	3948.0480	9.67	this study
CH_PR140080_TG012902_V0300	3962.8077	18.47	this study
CH_PR140080_TG012602_V0300	3964.2625	10.12	this study
CH_PR140080_TG012402_V0300	3969.1066	7.45	this study
CH_PR140080_TG012501_V0300	3975.4352	8.34	this study

Notes. Log of the 60 CHEOPS visits used in this study.